Protoplanetary Disks in ρ Ophiuchus as Seen from ALMA

Erin G. Cox[1] , Robert J. Harris[1,2] , Leslie W. Looney[1] , Hsin-Fang Chiang[2] , Claire Chandler[3] , Kaitlin Kratter[4] ,
Zhi-Yun Li[5], Laura Perez[6] , and John J. Tobin[7,8]

[1] Department of Astronomy, University of Illinois at Urbana-Champaign, Urbana, IL 61801, USA; egcox2@illinois.edu
[2] National Center for Supercomputing Applications, Urbana, IL 61801, USA
[3] National Radio Astronomy Observatory, P.O. Box O, Socorro, NM 87801, USA
[4] Department of Astronomy and Steward Observatory, University of Arizona, Tucson, AZ 85721 USA
[5] Department of Astronomy, University of Virginia, Charlottesville, VA 22903, USA
[6] Max Planck Institute for Radio Astronomy, Bonn, D-53121, Germany
[7] Homer L. Dodge Department of Physics and Astronomy, University of Oklahoma, Norman, OK 73019, USA
[8] Leiden Observatory, Leiden University, P.O. Box 9513, 2000-RA Leiden, The Netherlands

Abstract

We present a high angular resolution ($\sim$0.″2), high-sensitivity ($\sigma \sim 0.2$ mJy) survey of the 870 μm continuum emission from the circumstellar material around 49 pre-main-sequence stars in the ρ Ophiuchus molecular cloud. Because most millimeter instruments have resided in the northern hemisphere, this represents the largest high-resolution, millimeter-wave survey of the circumstellar disk content of this cloud. Our survey of 49 systems comprises 63 stars; we detect disks associated with 29 single sources, 11 binaries, 3 triple systems, and 4 transition disks. We present flux and radius distributions for these systems; in particular, this is the first presentation of a reasonably complete probability distribution of disk radii at millimeter wavelengths. We also compare the flux distribution of these protoplanetary disks with that of the disk population of the Taurus–Auriga molecular cloud. We find that disks in binaries are both significantly smaller and have much less flux than their counterparts around isolated stars. We compute truncation calculations on our binary sources and find that these disks are too small to have been affected by tidal truncation and posit some explanations for this. Lastly, our survey found three candidate gapped disks, one of which is a newly identified transition disk with no signature of a dip in infrared excess in extant observations.

Key words: protoplanetary disks – stars: formation – stars: pre-main sequence

1. Introduction

In recent years, there has been an explosion in the detections of extra-solar planets. As of early 2017, there are nearly 3000 exoplanets confirmed and another 2500 candidate exoplanets (e.g., exoplanets.org). These planets show a great diversity of properties, including masses, sizes, and architectures. In fact, many of these systems have planets that are unlike our solar system, such as super Earths, hot Jupiters, and hot Neptunes (Chiang & Laughlin 2013). The diversity of the planet population is likely some combination of differences in the initial conditions during the evolution of the circumstellar disk in which the planetary system forms and the necessary random interactions or scattering events during the planetary growth process (Bitsch & Kley 2011; Bitsch et al. 2015). To better understand the origin of the planet diversity, we therefore need to explore the inherent diversity in the circumstellar disks around young stellar objects (hereafter, YSOs). By directly observing the environments in which young planetesimals are expected to form, we can characterize the initial conditions of these other worlds.

To explore these early conditions, we must observe the protostar at the evolutionary phases that likely have the largest impact on planet evolution. While the exact phase is still unknown, the protostar must have evolved to the point where a large mass reservoir, i.e., a protoplanetary disk, surrounds the star. A protostar's evolutionary path can be divided into 4 parts- Class 0—III (e.g., Lada 1987; Andre et al. 1993; Dunham et al. 2014). During the initial collapse, i.e., the Class 0 phase, the protostar is engulfed in a large envelope full of

nascent dust and gas. By the Class I phase, most of the envelope material has been funneled onto the central protostar through a circumstellar disk. During the Class II phase, the protostar no longer has its nascent envelope surrounding it, and the majority of the circumstellar material is in a large disk. Lastly, during the final phase of the protostar, Class III, the protostar has essentially accreted all of its final mass, leaving a very tenuous (if any) circumstellar disk left (e.g., Andrews & Williams 2005a, 2007).

It is well known that planets form in the disk surrounding forming protostars, and it is commonly thought that most planet formation happens during the Class II phase of evolution. This is due to the fact that, by this time, the majority of the remaining gas and dust are surrounding the central protostar in a disk, allowing a large reservoir for planetesimals to form and evolve. While there is overwhelming indirect evidence for planet formation in disks, direct imaging of forming protoplanets has been scarce, with few examples in the literature (LkCa 15, Kraus & Ireland 2012; FW Tau; ROXs 12; ROXs 42B, Kraus et al. 2014). However, recent Atacama Large Millimeter/submillimeter Array (ALMA) observations of protoplanetary disks are beginning to reveal likely indicators of ongoing planet formation, such as the gaps in the millimeter disks of HL Tau (ALMA Partnership et al. 2015), a Class I/II protostar, and of TW Hydra (Andrews et al. 2016), a Class II protostar.

ρ Ophiuchus is an ideal laboratory for studying star and planet formation for several reasons. First, it is relatively close ($d \sim 137$ pc; Ortiz-León et al. 2017); second, it is relatively young (between 0.5 and 2 Myr; Wilking et al. 2008); finally, it has a large number of confirmed/candidate members ($\gtrsim$300;

Wilking et al. 2008). Despite these advantages, there are few millimeter-wave studies of its disk population that are representative of the disk content of Oph. One reason for this is that the stellar population is not well-characterized or studied: with A_v ranging from 1 to 100 across the cloud, an accurate/representative stellar census has not been possible to date, despite many optical/IR surveys of different parts of the cloud (see, e.g., Barsony et al. 2003 and references therein), making connections to host star properties difficult. Another reason is that Oph lies far in the southern hemisphere, making it somewhat challenging to observe with northern instruments.

Of the few large-scale surveys toward Oph, most have been done with single-dish telescopes, and thus are potentially compromised by cloud contamination, companion stars, etc. The first studies of the Oph cloud core (Andre et al. 1990; Leous et al. 1991) showed an abundance of millimeter/ centimeter-bright, deeply embedded objects residing in the dense core. Subsequent systematic studies of both the cloud core and surrounding regions (Andre & Montmerle 1994; Andrews & Williams 2007) demonstrated that millimeter flux tends to decline with class, signifying circumstellar mass depletion during evolution (either through accretion or outflow or dispersion, by, e.g., photo-evaporation), and also that the millimeter spectral index tends to decline as well, most likely indicating grain growth in the circumstellar dust (e.g., Ricci et al. 2010).

Subsequent work at high resolution with both the Submillimeter Array (SMA) and ALMA have yielded more details by probing the disk structures in Oph at sub-arcsecond resolution. These studies have, however, focused principally on either the detailed structure of the transitional disk population of Oph (Andrews et al. 2009, 2010; Pérez et al. 2014) or other special (i.e., bright) objects (Pérez et al. 2012; Salyk et al. 2014). Despite these studies of special subpopulations of Oph disks, there has, to date, been no systematic study at high resolution ($<0\overset{\prime\prime}{.}2$) of the disks of the ρ Ophiuchi cloud complex. In this article, we present the results from our ALMA 870 μm survey of $\sim$50 evolved disks in ρ Ophiuchus.

2. Sample Selection

One of the main goals of this program is to observe the compact disk dust emission toward a large sample of sources that does not have the inherent biases of previously known millimeter flux detections. To achieve such a large and representative sample of sources, we used the *Spitzer* c2d catalog of YSO candidate sources in ρ Ophiuchus (Evans et al. 2003), which requires S/N $\geqslant$ 3 in all the 4 IRAC bands and the 24 μm MIPS band. This criterion yields 297 protostellar sources. To increase the likelihood of detectable circumstellar mass (i.e., long-wavelength dust emission), we narrowed the sample to sources with 70 μm MIPS band detection S/N > 2. This requirement removed mostly the older source population (e.g., Class III objects based on SED fitting between 2 and 24 μm) and other sources that have low-mass disks due to other factors (i.e., environment, system mass, etc.), including 18 Flat and 10 Class I sources, which left 64 sources.

Finally, as this project is focusing on the more evolved sources without significant envelope emission, we also removed the sources that were known embedded sources from Young et al. (2006). This resulted in a total of 50 sources in our sample. These sources were then compared to Herschel PAC continuum maps at 70 and 100 μm to verify that the sources all had far-infrared emission. While doing this, it was realized that one of the sources was a clear galaxy (J163524.3-243359) and another was offset by exactly 1 arcmin (J162646.4-241160), which was likely a typo in the c2d catalog and is now corrected. The final source list of 49 sources, with their YSO class from the c2d catalog, is given in Table 1.

Because we select for sources that have infrared excesses in each of the IRAC and MIPs bands, we preferentially observe sources with a substantial disk reservoir. Since mass estimates at longer wavelengths are less affected by optical depth than those at shorter wavelengths, we attempt to quantify this bias by computing model disk fluxes at 70 μm and comparing them to the observed MIPS 70 μm fluxes in our sample. To do this, we assume the standard analytic prescription for a viscously evolving, geometrically thin disk (Lynden-Bell & Pringle 1974; Hartmann et al. 1998), a radial power law in temperature, and a power law in frequency for the total (i.e., gas + dust) opacity (Hildebrand 1983), i.e.,

$$\Sigma(r) \propto \left(\frac{r}{r_c}\right)^{-\gamma} \exp{-\left(\frac{r}{r_c}\right)^{2-\gamma}}$$

$$T(r) = T_{1\,\mathrm{au}}\left(\frac{r}{1\,\mathrm{au}}\right)^{-q}$$

$$\kappa_\nu = 0.03\left(\frac{\lambda}{870\,\mu\mathrm{m}}\right)^{-\beta}\,\mathrm{cm}^2\,\mathrm{g}^{-1},$$

with $T_{1\,\mathrm{au}}$ = 280 K, q = 0.5, β = 1, r_c = 100 au, and γ = 1. These values and expressions are roughly appropriate for these disks as observed in the (sub-)millimeter (e.g., Hughes et al. 2008; Andrews et al. 2009, 2010), although their applicability to the mid/far-infrared is uncertain. The median uncertainty for the c2d survey of Ophiuchus at 70 μm is approximately 25 mJy, so our 70 μm selection criteria selects sources with fluxes in excess of $\sim$50 mJy at 70 μm. Using these relations, we estimate that our sources all have $\gtrsim$0.2–1 Jupiter mass worth of circumstellar material (gas + dust), depending on the exact values for the quoted values above, as well as the relatively uncertain gas-to-dust ratio used for the computation of the opacity.

Out of the 49 targets selected, 12—ROph 2, 4, 6, 8, 11, 19, 21, 24, 26, 32, 36, and 50—were identified by Cieza et al. (2010) to be candidate transitional disks on the basis of *Spitzer* near-/mid-infrared colors; 11 sources—ROph 6, 8, 12, 13, 17, 18, 20, 21, 22, 23, and 46—were identified by Rebollido et al. (2015) on the basis of *Spitzer/Herschel* mid-/far-infrared colors. Three of these—ROph 6, 8, and 21—were identified on the basis of both, yielding 20 total infrared-identified transition disks in our sample. Of these 20 total transitional disk candidates three, ROph 2, 12, and 36, were discovered by Ruíz-Rodríguez et al. (2016) to harbor tight stellar binaries ($a \lesssim 3$ au), whose infrared signature mimicked that of transitional disks, and one, ROph 32, was discovered by Kohn et al. (2016) to be a spectroscopic binary with $a \sim 0.6$ au. ROph 6 was found to be a very tight ($\sim$5 mas) binary by Loinard et al. (2008); its mid-infrared color is due to the presence of a hot ring of material at a large distance from the star, and is most likely not indicative of a true transitional disk. This leaves 14 candidates that are "bona fide" transition disks with no evidence of being binary interlopers; see Table 2.

One caveat to keep in mind for this survey is the impact of unresolved (or unknown) multiplicity on the targets. ρ Ophiuchus

Table 1
Multiplicity of Target Sources

Known Singles			Known Binaries				
Field Name	Alt Name	References	Field Name	Alt Name	Separation (arcsec)	PA (°)	References
ROph3	IRAS 16201-2410	(e)	ROph2	V 935 Sco	0.02	…	(d)
ROph4		(e)	ROph5	WSB 19	1.49	262.9	(a)
ROph8	DoAr 25	(a), (c)	ROph6	DoAr 21	∼0.005	…	(g)
ROph9	El 24	(a), (b), (c)	ROph7	DoAr24 E	2.03	150	(a)
ROph10	GY 33	(a)	ROph12	WSB 40	0.017	…	(d)
ROph14	GY 211	(c)	ROph21	SR 9	0.638	353.3	(a)
ROph15	GY 224	(a), (b)	ROph26	ROXs 42C	0.277	151	(a)
ROph16	GY 235	(a)	ROph27	WSB 71	3.56	35.0	(a)
ROph17	GY 284	(a)	ROph32	WSB 74	≲0.043	…	(e)
ROph18	YLW 47	(a), (c)	ROph33	DoAr 51	0.784	79.3	(a)
ROph19	DoAr 33	(a), (c)	ROph34	L1689-IRS7	7.56	334.9	(h)
ROph20	GY 314	(a), (c)	ROph36		0.025	…	(d)
ROph22	SR 20 W	(a), (c)	ROph45	IRS 54	7.17	323.1	(b)

Known Singles			Known Triples				
ROph24	WSB 63	(a), (c)	Field name	Alt Name	Separation (arcsec)	PA(°)	References
ROph25	WSB 67	(a)	ROph11	WSB 38 Aa-Ab	0.098	24.2	(a)
ROph29	DoAr 44	(a), (c), (f)		WSB 38 Aab-B	0.577	105.4	(a)
ROph35	Haro 1-17	(a)	ROph13	SR 24 Aab	0.197	84	(a)
ROph40		(a)		SR 24 Aab-B	5.065	349	(a)
ROph41	WL6	(a), (b)	ROph23	SR 13 Aa-Ab	0.013	…[a]	(a)
ROph42	GY 312	(b)		SR 13 Aab-B	0.399	96	(a)
ROph43		(b)	ROph31	L1689-IRS5 A-Bab	3.0	241	(a)
ROph44	GY 344	(b)		L1689-IRS5 Ba-Bb	0.14	84.4	(a)
ROph46	WSB 60	(a)					
ROph48	IRS 63	(a)					
ROph50	Haro 1-11	(a), (c)					

No Data on Companion Objects			
Field Name	Alt Name	Field Name	Alt Name
ROph1		ROph39	
ROph28		ROph47	
ROph30		ROph49	
ROph38	WSB 82		

Note.
[a] Binary orbits with a period of ∼years, so the position angle depends sensitively on observation epoch.
References. (a) Ratzka et al. (2005), (b) Duchêne et al. (2004), (c) Cheetham et al. (2015), (d) Ruíz-Rodríguez et al. (2016), (e) Kohn et al. (2016), (f) Willson et al. (2016), (g) Loinard et al. (2008), (h) This work.

has been the target of several optical and infrared surveys of varying completeness in the past three decades, both targeting Class I/Flat (Barsony et al. 2004; Duchêne et al. 2004, 2007; Haisch et al. 2004, 2006) and Class II (Ghez et al. 1993; Ratzka et al. 2005) sources. It is known that stellar companions can have a dramatic effect on circumstellar material via tidal interactions that preferentially strip away outer disk material in circumstellar disks and inner disk material in circumbinary disks (Artymowicz & Lubow 1994; Pichardo et al. 2005, 2008). Observationally, truncation manifests as a decreased likelihood of an infrared excess in multiple systems as opposed to isolated stars (reflecting the absence of an inner disk; Cieza et al. 2009; Kraus et al. 2011) or decreased millimeter-wave continuum emission (reflecting loss of material in either the inner or outer disk; Jensen et al. 1994; Harris et al. 2012). Such signatures, if unrecognized, can bias the results of infrared and millimeter surveys of protoplanetary disks.

To mitigate the effect of this in our sample, we have surveyed the available literature on multiplicity in Ophiuchus to identify which of our targets are multiple systems.

Unfortunately, the principal surveys we used provide different sensitivities to various separations on the sky and give fairly heterogeneous coverage. Ratzka et al. (2005) conducted a magnitude-limited ($K \leqslant 10.5$) speckle imaging survey of 158 principally Class II objects and is sensitive to companions with separations between roughly 0″.1 and 6″.4, down to a contrast ratio of 0.1. Duchêne et al. (2004, 2007) conducted a direct imaging survey of principally Class I/Flat objects in the mid-infrared, with coverage ranging from 0″.8 to 10″.0. Because most surveys are flux-limited, several of the lower-luminosity sources in our sample have not been observed in these surveys. Of the 49 sources in our sample, 10 have not been observed in any available survey (ROph1, 3, 4, 28, 30, 38, 39, 42, 47, 49). Table 1 summarizes the multiplicity status of each system in our sample.

3. Observations and Data Reduction

The ALMA Band 7 observations were taken under proposal 2013.1.00157.S using a continuum-only setup to maximize the dust continuum sensitivity in two configurations for the

Table 2
Transition vs. Non-transition Disks

Not Transition Disks Based on N/FIR Colors			Objects with Transition Disk Colors or Millimeter Cavities			
Field Name	Alt Name	IR Band/Ref	Field Name	Alt Name	Band/Ref	True Disk or Binary/Ref
ROph1		N (a)	ROph2	V 935 Sco	N (a)	CB (2)
ROph5	WSB 19	N (a)	ROph 3[b]	IRAS 16201-2410	N, S (c, f)	T (3)
ROph7	DoAr 24 E	N (a)	ROph4		N (a)	T (3)
ROph9	EI 24	N, M (a, b)	ROph6	DoAr 21	N, M (a, b)	CB (4)
ROph10	GY 33	N (a)	ROph8	DoAr 25	N, M (a, b)	T (2, 3)
ROph14	GY 211	N (a)	ROph11	WSB 38	N (a)	T (3)
ROph15	GY 224	N (a)	ROph12	WSB 40	M (b)	T (2)
ROph16	GY 235	N (a)	ROph13	SR 24	M,S (b, d)	T (2)
ROph25	WSB 67	N (a)	ROph17	GY 284	M (b)	T (7)
ROph27	WSB 71	N (a)	ROph18	YLW 47	M (b)	T (5)
ROph28		N (a)	ROph19	DoAr 33	N (a)	T (2, 3, 5)
ROph30		N (a)	ROph20	GY 314	M (b)	T (5)
ROph31	L1689-IRS5	N (a)	ROph21	SR 9	N, M (a, b)	T (3, 5)
ROph33	DoAr 51	N (a)	ROph22	SR 20 W	M (b)	T (5)
ROph34	L1689-IRS7	N (a)	ROph23	SR 13	M (b)	CB (1)
ROph35	Haro 1-17	N (a)	ROph24	WSB 63	N (a)	T (2, 3, 5)
ROph39		N (a)	ROph26	ROXs 42C	N (a)	T (5)
ROph40	ISO-Oph 51	N, M (a, b)	ROph29[a]	DoAr 44	S (e)	T (2, 5, 6)
ROph41	WL 6	N (a)	ROph32	WSB 74	N (a)	CB (3)
ROph42	GY 312	N (a)	ROph36		N (a)	CB (2)
ROph43		N (a)	ROph38	WSB 82	S (f)	T (7)
ROph44	GY 344	N (a)	ROph46	WSB 60	M (b)	T (7)
ROph45	IRS 54	N (a)	ROph50	Haro 1-17	N (a)	T (7)
ROph47		N (a)				
ROph48	IRS 63	N (a)				
ROph49		N (a)				

Notes. Abbreviation key: N—near/mid-infrared colors; M—mid/far-infrared colors; S—(sub)mm-wave imaging of cavities; T—no indication of interloping circumbinary disk; CB—indication that a disk is circumbinary, not transitional.

[a] This source was classified as a pre-transitional disk by Espaillat et al. (2010) but did not meet the color criterion to be a transitional disk according to Cieza et al. (2010). We treat it as a non-transition disk here, for consistency.

[b] This source was classified as a transitional disk on the basis of *Spitzer* IRS spectra by Furlan et al. (2009), but as with ROph 29, the colors did not meet the criteria of Cieza et al. (2010).

References. (a) Cieza et al. (2010), (b) Rebollido et al. (2015), (c) Furlan et al. (2009), (d) Andrews & Williams (2005b), (e) Andrews et al. (2009), (f) this work, (1) Ratzka et al. (2005) (2) Ruíz-Rodríguez et al. (2016), (3) Kohn et al. (2016), (4) Loinard et al. (2008), (5) Cheetham et al. (2015), (6) Willson et al. (2016), (7) assumed transition based on lack of data.

snapshot survey. The lower-resolution observations were obtained on 2015 April 4 in ALMA configuration C34-1/(2) for ~30 minutes of total time, which was about 12 s of integration time on each source. The C34-1/(2) configuration baselines ranged from 14 to 356.3 m with typical recoverable scale of 8″.4. The higher resolution observations were obtained on 2015 July 24 in ALMA configuration C34-7/(6) for ~47 minutes of total time, which was about 24 s of integration time on each source. The C34-7/(6) configuration baseline ranges from 42 to 1574 m, with a typical recoverable scale of 2″.6. In both observations, the 4 continuum bands were centered at 336.5, 338.4, 348.5, and 350.5 GHz. The quasars J1517-2422 and J1625-2527 were used for bandpass and phase calibration, and Titan was used for flux calibration. In this paper, we assume an absolute flux calibration uncertainty of ~10%, but only statistical uncertainties are considered.

The observations were reduced using the Common Astronomy Software Applications (CASA) package (McMullin et al. 2007) using the 4.7.0 CASA and ALMA pipeline package. Briefly, the pipeline first applies a priori calibrations, such as baseline corrections and phase corrections, from water vapor radiometer measurements. Then, it conducts a standard interferometric reduction: bandpass calibration, flux calibration, and antenna gain calibrations. These calibrations are performed separately for each of the two observations and each science target field was subsequently split out of its parent data set. For the C34-1/(2) configuration observations, we performed a phase-only selfcal over the integration time for the sources with $\geqslant 10\sigma$ detections to improve the S/N in the maps. The C34-7/(6) configuration map S/N was not improved from selfcal, so the selfcal gains were not used. After the final images were made for each configuration, we checked to ensure that the fluxes measured for each observation were consistent; finding that they were, we combined the two data sets and used the combined data sets to produce the images analyzed in this work.

To produce the final images, we imaged the data using the CLEAN task in CASA. The data were imaged with natural weighting to produce a typical resolution of 0″.21 by 0″.18. Many of our sources are relatively compact (see Figures 1 and 2) and standard CLEAN was sufficient to deconvolve the sources successfully. However, for many of the more extended disks, standard CLEAN left substantial deconvolution errors in the residual maps, so we used the multi-scale version of the algorithm to produce images of some of the disks in Figures 1 and 3 as well as all of the transition disks in our sample

Table 3
Statistics of Different Populations

Comparison	Flux p-value	Radius p-value
Singles and Binaries	0.06946	0.01766
Singles and Binaries (no circumbinary disk)	0.00876	0.00075
Singles and Triples	0.73140	0.03613
Singles and Multiples	0.11562	0.00368
Singles and Transition Disks	0.10204	0.04363
Binary Components	0.21271	0.15456
Binary Components (no circumbinary disk)	0.53125	0.15456
Class II and Class I/Flat	0.24451	0.79303

Population	Median Flux (mJy)	Median Radius (au)
Singles	46.3	17.9
Binaries	27.74	7.1
Binaries (no circumbinary disk)	19.6	6.85
Bright Binary component	27.74	6.45
Bright Binary (no circumbinary disk)	21.29	6.17
Dim Binary component	6.17	7.54
Dim Binary (no circumbinary disk)	6.45	7.54
Triples	15.41	8.08
Multiples	19.6	7.8
Transition Disks	262	62.34
Class I/Flat Sources	30.55	12.6
Class II Sources	18.73	13.426

Note. Comparison of the various p-values obtained from each CDF. Note that "multiples" represents a combination of both binary and triple systems. We used a distance of 137 pc to compute the radius.

(Figure 4). The use of the multi-scale CLEAN algorithm yielded residual maps that were dominated by Gaussian noise.

4. Results

This survey provided very well-resolved images of the diverse population of protoplanetary disks in ρ Oph YSOs. Figures 1–4 show the different YSOs divided into single sources, binaries, triple systems, and transition disks. The sources that do not have multiplicity information are considered single, unless they show evidence of being a transition disk. Since transition disks are separated into their category, we do not include them in any other categories (i.e., singles or triples). Each figure uses the same stretch for flux values, such that the brightest sources show the deepest red color. At a glance, it is obvious that our sample is not only composed of different types of systems, but also each type shows great diversity in size, brightness, and flux distribution. In the 49 stellar systems that we targeted, there were 63 stars, and disks associated with 13 stars were not detected: 4 around single stars, 4 around components of binaries, and 5 around components of triple systems. Table 4 summarizes this information for all sources, including classifications of the YSOs from c2d. The disk sizes and position angles, as well as the peak and integrated fluxes, were estimated by fitting a Gaussian in the image plane using the CASA task imfit. Disk masses were estimated from the integrated fluxes by assuming optically thin emission and an isothermal disk with a dust temperature of $T_d = 20$ K, i.e.,

$$M_d = \frac{F_\nu d^2}{\kappa_\nu B_\nu(T_d)},$$

where F_ν is the integrated flux at 870 μm, d is the estimated distance to Ophiuchus (137 pc), $\kappa_\nu = 0.03$ cm^2 g^{-1} is the total opacity at 870 μm assuming a Hildebrand (1983) dust opacity and a 100:1 gas-to-dust ratio (Bohlin et al. 1978), and B_ν is the Planck function. An important caveat here is that this mass calculation is only an estimate at best. Recent studies have suggested that the gas mass might be considerably lower than the often prescribed 100:1 ratio (Williams & Best 2014).

To test for significant differences in flux and radius among the different subpopulations of our sample, we used the implementation of the Kaplan–Meier (KM) product estimator in the lifelines Python package (Davidson-Pilon et al. 2017)[9] to estimate the cumulative distribution functions (CDFs) for all of the subpopulations (see Figures 5–12). The KM estimator is akin to an empirical cumulative probability distribution, but it has the advantage of being able to account for the non-detections in our sample by incorporating σ upper limits when appropriate. For all the distributions we compute for fluxes, upper limits are incorporated. However, for the radii KM estimators, we only incorporate detections, as the radius of a non-detected object is ill-defined. Confidence intervals for each bin in the KM estimator are computed using Kalbfleisch and Prentice's modification of the result of Greenwood (1926; see p. 18 of Kalbfleisch & Ross 2002 for details).

After the KM estimators are computed for each subpopulation, we use the non-parametric log-rank test to determine whether or not it is likely that the two cumulative distributions in flux or radius are different for the pairwise combinations of subpopulations. Figure 5 shows the CDFs comparing the flux of the single sources in our survey with the fluxes of the other populations (binaries, triples, multiples, and transition disks). Perhaps the most striking feature of these comparisons is that of the binary population. The binary sources in this survey show systematically lower flux values than the isolated population.

In Table 3 we report the p-values of the different comparisons, as well as the median flux and radius of the different populations. The p-value represents the probability that, given our data, the two populations compared are drawn from a single distribution. Thus, the higher our p-value, the more likely that this is the case; conversely, the lower the p-value, the less likely it is for the two populations to be from the same distribution. We define two populations to have a significant difference if the log-rank on their respective KM estimators yields $p \lesssim 0.05$.

When comparing the binaries with the singles, we find that both the flux and radius p-values show a suggestive trend with both p-values <0.1 ($p_{\rm flux} = 0.06946$ and $p_{\rm radius} = 0.01766$). Our binary sample includes three circumbinary disks (disks that encompass both components of the binary system) that we find to be quite bright compared to the rest of the binary sample. Since Harris et al. (2012) also found this to be true in Taurus, we looked at the same comparison without these sources. We find that without the circumbinary disks, we get $p_{\rm flux} = 0.00876$ and $p_{\rm radius} = 0.00075$, which is lower

---

[9] This package is available at https://github.com/CamDavidsonPilon/lifelines/.
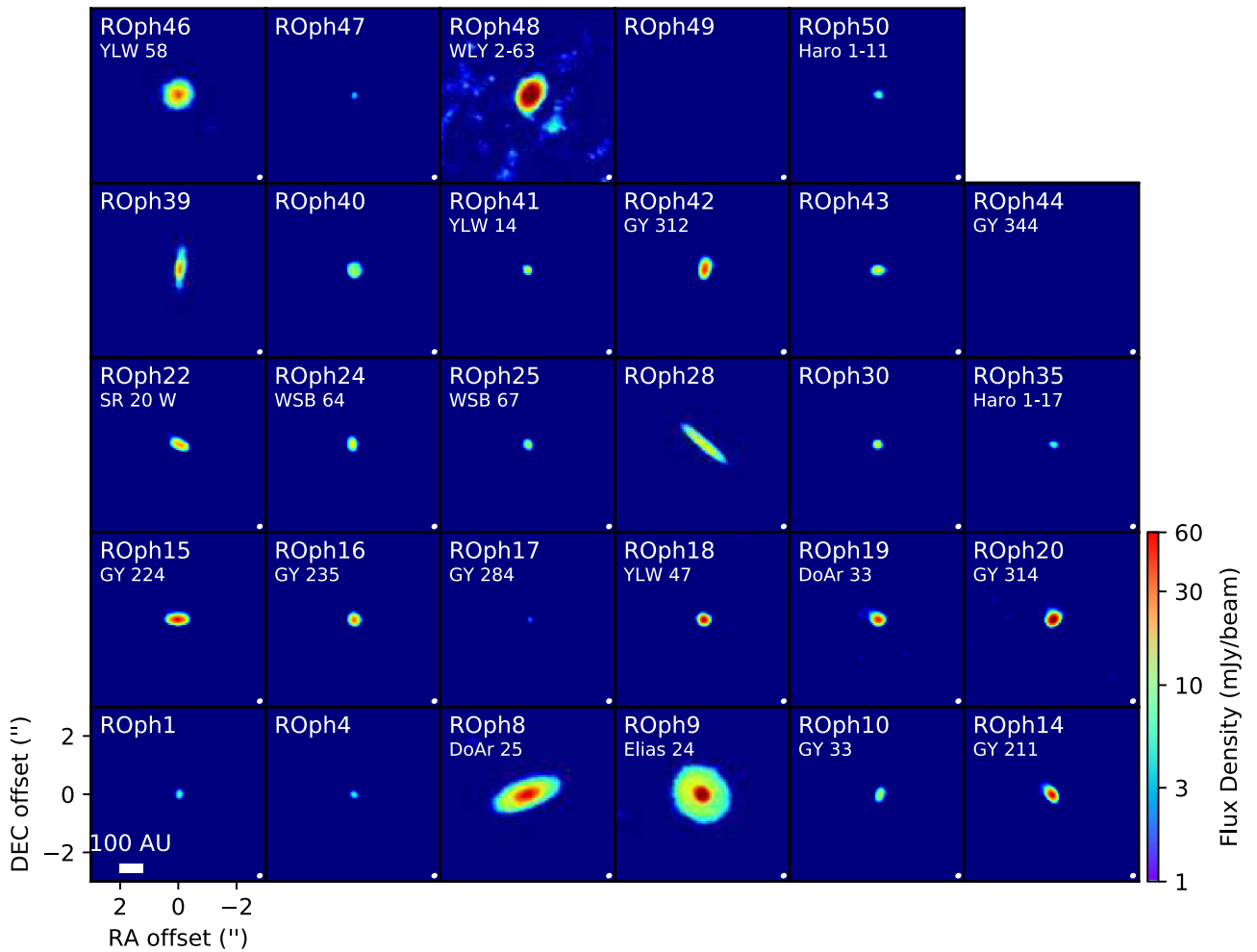
Figure 1. Images of the single sources in our sample. The synthesized beam is shown in the bottom right corner. ROph1, 3, 4, 28, 30, 39, 42, and 47 have not previously been observed in any survey. Note that the flux scale on the right is a constant scaling for these images. This figure has been updated to reflect the new multiplicity table.

than our cutoff. Figures 5 and 6 show the CDF comparing the two populations in the top left panel for flux and radius, respectively, and Figure 7 shows the same plot, but excluding circumbinary disks. Each binary component was counted as one source, and in the case of a non-detection, the 3σ value of the map was used as an upper limit for fluxes. All known, non-spectroscopic, (i.e., Oph 6, 12, 32, and 36) binaries in our sample are resolved, therefore blending of component fluxes is not an issue in our sample. It can be visually seen in these plots (see the top left panel of both Figures 5–7), that there is hardly any overlap between the isolated YSOs and the binaries. The binary components are systematically dimmer (and smaller) than their isolated counterparts. In Figure 8, we show the comparison between the components of the binary YSOs. The brighter component has a median flux value of 27.74 mJy, while the dimmer component is at 6.45 mJy. This a factor of 5 different, although we note that the large uncertainty in each individual bin of the KM estimator makes any observed difference between the populations not significant. The difference in the median radius for either component is <2 au, meaning that there is not a discernible difference in the sizes of the two.

Across star-forming regions, the inner disk fraction for single stars and for wide binaries (i.e., binaries with projected separation >40 au) is comparable, with ∼50% of these

systems harboring enough material to make them Class II objects. On the other hand, tighter systems (<40 au) are preferentially less likely to have evidence of an infrared excess, with only ∼20% of those systems harboring enough material to make them Class II objects (Cieza et al. 2009). Folding these data into our analysis of the millimeter emission for singles versus binaries would most likely make the difference between the two much starker.

The triple systems in our sample are slightly more complicated than the binaries. Two of the three systems (ROph11 and ROph31) are treated in the same way as the binaries, where we use the 3σ value for the non-detections. The third system, ROph23, is also treated in this way; however, this system has a circumbinary disk. Since this cannot be divided into two different systems, we count this as one source and use the 3σ value of the map as the upper limit twice. When comparing these with the singles, we find $p_{\text{flux}} = 0.73140$ and $p_{\text{radius}} = 0.03613$. A caveat to keep in mind when looking at the triple systems in this sample, is that we did not detect all three sources in any of the systems. These systems consist of a tight pair that will resemble binary systems, with a single star further away. In ROph 11 and in ROph 31, the distance of the third component from the tight pair is much larger than the separation of the tight pair itself. Therefore, the disk associated with the distant object more closely resembles a disk from a
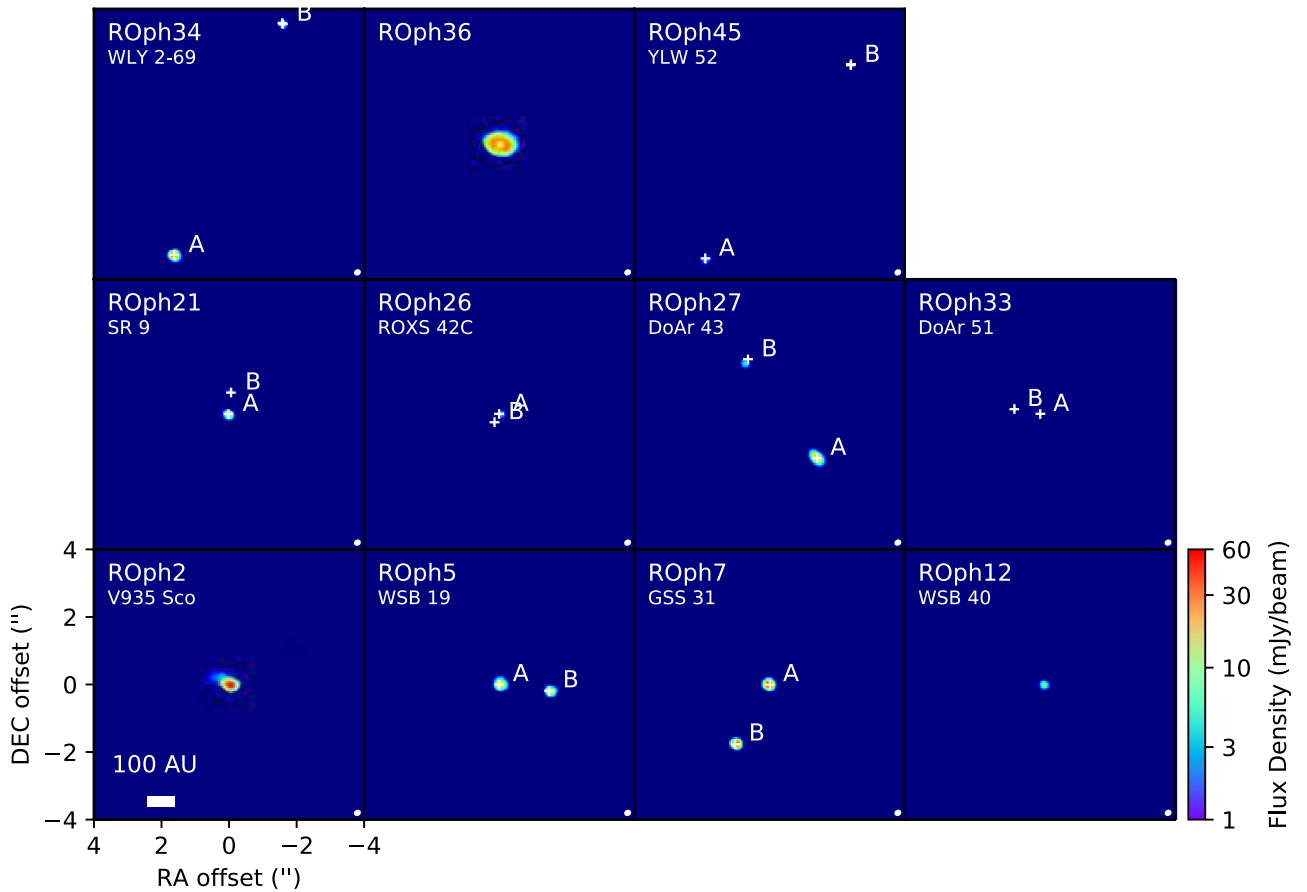
Figure 2. Images of the binary sources in our sample. The synthesized beam is shown in the bottom right corner. Stellar positions are indicated by white crosses. This figure has been updated to reflect the new multiplicity table.
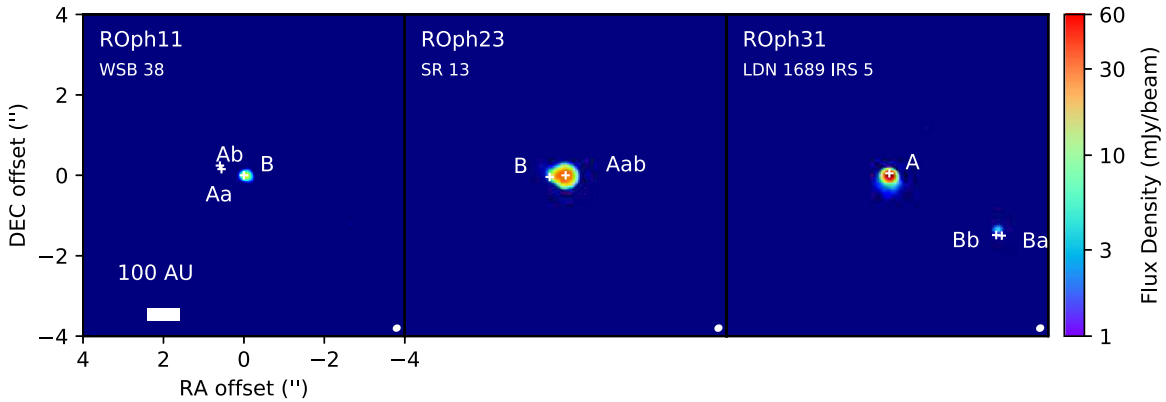

Figure 3. Image of the triple systems in our sample. The center panel shows ROph23 with an asymmetrical, circumbinary disk surrounding Aab. The synthesized beam is shown in the bottom right corner. Stellar positions are indicated by white crosses. This image was not changed in the update to the current multiplicity table.

single source. This is likely the case in ROph 23 as well, though the orbit superimposes the distant companion onto the circumbinary disk.

The transition disks we used in comparing with the isolated sources were ones that show a depletion of millimeter emission in their inner cavity in this data set, not necessarily those listed in Table 2. Visually, our transition disk population (see Figure 4) seems to be the most unique in both flux and size. It was somewhat surprising that the fluxes of these disks did not show $p < 0.05$ when compared to the singles ($p_{\mathrm{flux}} = 0.10204$ and $p_{\mathrm{radius}} = 0.04363$). We only have four transition disks in our sample, so the small numbers may contribute to the higher

p-values. The median flux for this population is a factor of 5 brighter than any other population and the median radius is 3.5 times as large as the isolated population, suggesting that the transition disks come from a different distribution. We did use the two different populations of Table 2 to see if there was anything statistically different between sources that either have sub-/millimeter cavities or infrared colors indicating they are transition disks, and those that do not. We find $p_{\mathrm{flux}} = 0.12846$ and $p_{\mathrm{radius}} = 0.09715$.

Figure 10 shows the CDF plots for the different classifications of YSOs. Our sample consisted of mostly Class II YSOs, followed by Flat and then Class I objects. Since the Flat sources
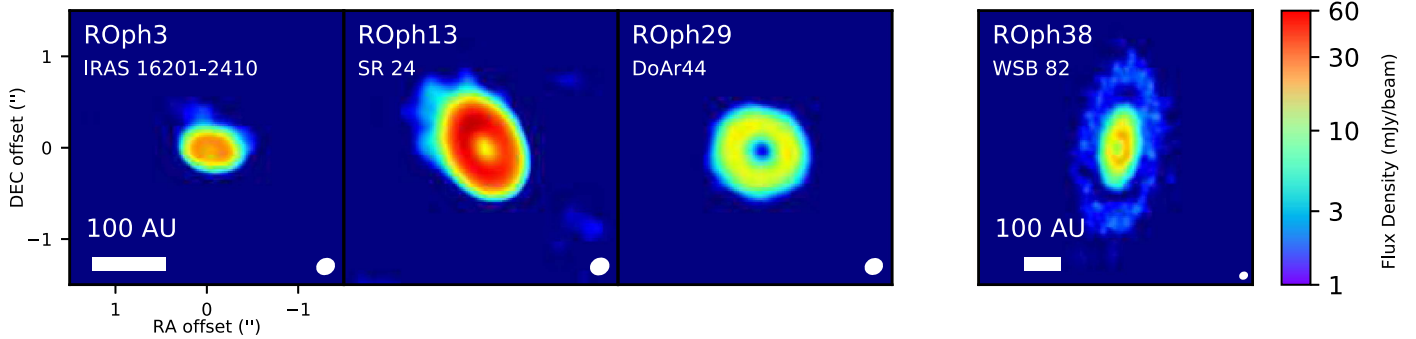
Figure 4. Images of four transition disks with substantial millimeter cavities in our sample. The source on the right (ROph 38) is a particularly large transition disk, with a low-level emission gap. This source has also not previously been observed in any sub/mm-wave survey. The synthesized beam is shown in the bottom right corner. This image has been updated to the current multiplicity table.

are thought to be on average less evolved than the the Class II sources, we combined these with the Class I sources to more easily compare the two. The less evolved population shows a higher (∼13 mJy) median flux, while also having a slightly lower (∼1 au) median radius. This is as expected, since as the YSO evolves into a Class II object, its peak energy output moves to shorter wavelengths (Lada 1987) and, as the nascent material from the envelope falls in, the disk surrounding the protostar will grow (Dunham et al. 2014).

We report the detection of a ∼1600 au millimeter-wave companion to ROph34, L1689-IRS 7. The system L1689 IRS 7 has only sparsely been surveyed for companions. It was included in the Ratzka et al. (2005) survey area, but the source was determined to be single. The separation regime that the Ratzka survey was sensitive to ranged from 0.1 to 6.4 arcsec, and the companion that we report is located outside of 7 arcsec. The companion can be seen in 2MASS. The JHK_s magnitudes of the northern component are uniformly ∼2 mag lower than the corresponding magnitudes for the southern component $K_s \sim 8.5$ for the primary and 10.5 for the secondary. Since the colors are the same, it is likely that the companion is also a Class II low-mass star that is a bona fide member of the Oph complex. From the K-band contrast, we estimate a stellar mass ratio of 0.1–0.3 based on Seiss (2001) models for a 1 Myr old object (roughly consistent with the fact that the source is a Class II object).

5. Discussion

5.1. Comparison with the Taurus–Auriga Molecular Cloud

In this work, we have used ALMA to map the distribution of 870 μm emission from 49 selected pre-main-sequence stellar systems in the ρ Ophiuchus molecular cloud and used these maps to construct the distribution of disk fluxes and radii from various subpopulations. A natural question to ask is how the systems in one molecular cloud compare to those of another. To do this, we have compiled a target list of sources in the Taurus–Auriga molecular cloud to which we compare our sample. Taurus represents an obvious choice for such a comparison. First, it has a well-characterized stellar population and disk population due to its proximity (145 pc; Loinard et al. 2007; Torres et al. 2007, 2009), as well as a relatively uniformly low extinction across the whole cloud (Lombardi et al. 2010). Second, ρ Oph has a relatively low stellar density across much of its volume and very few UV/X-ray luminous O/B-type stars, much like Taurus and opposed to clusters such

as Orion. Such environmental impacts are known to have severe and deleterious effects on protoplanetary disk masses and radii (e.g., Mann et al. 2014). Finally, the two clusters are close to the same age: ρ Oph is between 0.5 and 2 Myr (Wilking et al. 2008) old, while Taurus is in the vicinity of 1–2 Myr old (Luhman et al. 2010).

In order to quantify how common our sample is, we have constructed a sample of Taurus sources to which we compare our Oph sample. To do this, we used the results of the *Spitzer* survey performed by Rebull et al. (2010). They surveyed approximately 44 square degrees of Taurus in each of the seven different IRAC/MIPS bands. To ensure that our comparison stars were in Taurus, we restricted our selection to the subsample of their survey that had already previously been identified as Taurus members, rather than those sources that were inferred to be Taurus members based on colors from their survey. As in our survey, we only included sources with detections in all of the IRAC bands as well as the 24 and 70 μm bands, in the same fashion as was done for our present survey. The sensitivities of the Rebull et al. (2010) survey are similar to those of the c2d survey, so this is probably a fair comparison. After selecting candidate sources in Taurus, we restricted the sample to those sources that had (sub)-millimeter flux information in the literature. Where multi-band photometry was available, we used the derived spectral index to infer the 870 μm flux density; where it was not available, we assumed that the intrinsic spectral index was 3. The qualitative results for this work do not depend on the precise value of α that we assume. We use the same KM estimators to compare the corresponding subpopulations of Taurus–Auriga objects with Oph objects. The p-values for these comparisons are found in Table 5.

In Figures 11 and 12 we show the CDF comparisons of the Oph and Taurus populations. We find that the single sources have different median fluxes (31 mJy versus 57 mJy), with their corresponding low p-value (0.00282) most likely due to the Taurus population having a high flux tail in its distribution. One possibility for this dichotomy is the difference in the environments between the two clouds. ρ Oph tends to have more clustered YSOs, while Taurus's YSOs are more dispersed. We find that Ophiuchus typically has dimmer binary and triple systems, as well as Class II protostars, with its Class I population being much dimmer (∼31 mJy versus ∼116 mJy) than that of Taurus. Due to the low number of Class I YSOs in our survey, this is likely due to small number statistics.

9

Table 4
Protoplanetary Disks in ρ Ophiuchus Molecular Cloud

Index	Object	Class	Derived Position (J2000)	Disk Size ($''$)	Disk PA ($°$)	Peak Flux (mJy beam^{-1})	Integrated Flux (mJy)	$M_{\rm disk}$ ($M_{\rm Jupiter}$)
1	2MASS J16213192-2301403	II	16:21:31.923–23:01:40.761	$0.193 \pm 0.015 \times 0.07 \pm 0.032$	164 ± 6.6	6.2 ± 0.21	9.63 ± 0.49	0.59
2[a,e]	V935 Sco	II	16:22:18.523–23:21:48.549	$0.215 \pm 0.011 \times 0.125 \pm 0.009$	80.5 ± 4.7	41.98 ± 0.89	72.9 ± 2.3	4.43
3[c]	IRAS 16201-2410	II	16:23:09.219–24:17:05.364	$0.456 \pm 0.043 \times 0.283 \pm 0.029$	81.4 ± 8.2	26 ± 1.8	114.3 ± 9.7	6.96
4	2MASS J16233609-2402209	II	16:23:36.113–24:02:21.227	$0.160 \pm 0.014 \times 0.072 \pm 0.016$	6.7 ± 6.5	5.27 ± 0.15	7.12 ± 0.31	0.43
5[a]a	WSB 19A	II	16:25:02.119–24:59:32.798	$0.198 \pm 0.011 \times 0.188 \pm 0.013$	145 ± 60	14.11 ± 0.27	27.74 ± 0.77	1.69
5[a]b	WSB 19B	II	16:25:02.011–24:59:33.004	$0.127 \pm 0.017 \times 0.107 \pm 0.019$	106 ± 39	14.45 ± 0.33	19.60 ± 0.7	1.20
6	DoAr 21	II	16:26:03.300–24:23:36.000	$\cdots \times \cdots$	$\cdots$	$\cdots$	<0.89	<0.05
7[a]a	GSS 31a	II	16:26:23.362–24:20:59.997	$0.100 \pm 0.004 \times 0.060 \pm 0.007$	169 ± 5	39.34 ± 0.21	46.75 ± 0.4	2.85
7[a]b	GSS 31b	II	16:26:23.432–24:21:01.749	$0.071 \pm 0.004 \times 0.051 \pm 0.008$	147 ± 15	34.67 ± 0.21	38.36 ± 0.38	2.33
8	DoAr 25	II	16:26:23.680–24:43:14.303	$1.071 \pm 0.038 \times 0.487 \pm 0.015$	110 ± 1.4	38 ± 1.2	515 ± 18	31.33
9[d]	Elias 24	II	16:26:24.078–24:16:13.855	$0.558 \pm 0.049 \times 0.474 \pm 0.042$	45 ± 81	63 ± 4.5	489 ± 39	29.77
10	GY 33	II	16:26:27.540–24:41:53.882	$0.337 \pm 0.013 \times 0.097 \pm 0.014$	160.5 ± 1.7	10.22 ± 0.27	23.45 ± 0.84	1.43
11[t]	WSB 38 Aa	II	16:26:46.471–24:12:00.39	$\cdots$	$\cdots$	<0.8	<0.8	<0.04
11[t]	WSB 38 Ab	II	16:26:46.474–24:12:00.30	$\cdots$	$\cdots$	<0.8	<0.8	<0.04
11[t]	WSB 38B	II	16:26:46.427–24:12:00.443	$0.086 \pm 0.013 \times 0.033 \pm 0.020$	108 ± 14	13.82 ± 0.2	15.41 ± 0.38	0.94
12[a,f]	WSB 40	II	16:26:48.651–23:56:34.589	$0.082 \pm 0.012 \times 0.056 \pm 0.018$	167 ± 32	7.78 ± 0.13	8.83 ± 0.24	0.53
13[b]	SR 24aa	II	16:26:58.438–24:45:32.24	$\cdots$	$\cdots$	<1.2	<1.2	<0.07
13[b]	SR 24ab	II	16:26:58.453–24:45:32.21	$\cdots$	$\cdots$	<1.2	<1.2	<0.07
13[b,c]	SR 24b	II	16:26:58.504–24:45:37.220	$0.984 \pm 0.118 \times 0.563 \pm 0.070$	22.5 ± 8.3	42.9 ± 4.7	624 ± 73	37.96
14	GY 211	II	16:27:09.096–24:34:08.708	$0.265 \pm 0.005 \times 0.127 \pm 0.004$	33.1 ± 1.2	45.79 ± 0.43	91.2 ± 1.2	5.55
15	GY 224	F	16:27:11.168–24:40:47.100	$0.428 \pm 0.009 \times 0.148 \pm 0.005$	92.23 ± 0.79	42.13 ± 0.62	126.2 ± 2.4	7.67
16	GY 235	F	16:27:13.813–24:43:32.053	$0.208 \pm 0.010 \times 0.172 \pm 0.010$	177 ± 13	26.18 ± 0.41	51 ± 1.1	3.11
17	GY 284	F	16:27:30.841–24:24:56.528	$\cdots \times \cdots$	$\cdots$	2.78 ± 0.11	2.79 ± 0.19	0.17
18	YLW 47	II	16:27:38.314–24:36:58.997	$0.155 \pm 0.005 \times 0.144 \pm 0.005$	105 ± 20	51.68 ± 0.39	82.73 ± 0.94	5.03
19	DoAr 33	II	16:27:39.004–23:58:19.149	$0.225 \pm 0.006 \times 0.176 \pm 0.005$	78.2 ± 5.6	37.68 ± 0.49	76.4 ± 1.4	4.64
20	GY 314	II	16:27:39.422–24:39:15.940	$0.258 \pm 0.005 \times 0.145 \pm 0.006$	138.9 ± 2.1	72.12 ± 0.86	151.9 ± 2.5	9.23
21[a]a	SR 9A	II	16:27:40.275–24:22:04.568	$0.073 \pm 0.016 \times 0.065 \pm 0.021$	69 ± 83	13.15 ± 0.26	14.83 ± 0.48	0.90
21[a]b	SR 9B	II	16:27:40.272–24:22:03.888	$\cdots \times \cdots$	$\cdots$	3.02 ± 0.036	3.02 ± 0.036	0.18
22	SR 20 W	II	16:28:23.337–24:22:41.070	$0.420 \pm 0.022 \times 0.145 \pm 0.011$	65.7 ± 1.7	22.16 ± 0.76	64.1 ± 2.9	3.90
23[b,d] Aab	EM* SR 13Aab	II	16:28:45.266–24:28:19.358	$0.412 \pm 0.040 \times 0.329 \pm 0.034$	90 ± 27	31.7 ± 2.2	148 ± 12	9.00
23[b]	EM* SR 13B	II	16:28:45.28–24:28:19.318	$\cdots$	$\cdots$	$\cdots$	<0.85	<0.04
24	WSB 63	II	16:28:54.071–24:47:44.694	$0.266 \pm 0.005 \times 0.107 \pm 0.006$	0.07 ± 1.28	15.53 ± 0.17	30.55 ± 0.48	1.86
25	WSB 67	II	16:30:23.398–24:54:16.511	$0.175 \pm 0.011 \times 0.112 \pm 0.013$	12.8 ± 8.4	10.83 ± 0.21	16.82 ± 0.49	1.03
26[a]a	ROXS 42Ca	II	16:31:15.738–24:34:02.487	$\cdots \times \cdots$	115.6 ± 3.7	3.96 ± 0.16	4.14 ± 0.18	0.25
26[a]b	ROXS 42Cb	II	16:31:15.748–24:34:02.72	$\cdots \times \cdots$	$\cdots$	<0.89	<0.89	<0.4
27[a]a	DoAr 43a	II	16:31:30.873–24:24:40.288	$0.267 \pm 0.008 \times 0.110 \pm 0.006$	38.3 ± 1.6	18.8 ± 0.28	36.29 ± 0.78	2.21
27[a]b	DoAr 43b	$\cdots$	16:31:31.025–24:24:37.484	$0.121 \pm 0.021 \times 0.111 \pm 0.025$	97 ± 85	4.83 ± 0.15	6.58 ± 0.32	0.40
28	2MASS J16313124-2426281	II	16:31:31.245–24:26:28.438	$1.301 \pm 0.029 \times 0.157 \pm 0.005$	49.05 ± 0.21	14.75 ± 0.25	124.8 ± 2.4	7.60
29[c]	DoAr44	II	16:31:33.455–24:27:37.515	$0.911 \pm 0.147 \times 0.821 \pm 0.134$	63 ± 59	12.4 ± 1.8	262 ± 41	15.99
30	2MASS J16314457–2402129	II	16:31:44.577–24:02:13.475	$0.110 \pm 0.007 \times 0.069 \pm 0.014$	133.8 ± 8.9	15.30 ± 0.16	18.81 ± 0.32	1.14
31[b]a	LDN 1689 IRS 5A	F	16:31:52.111–24:56:16.030	$0.117 \pm 0.013 \times 0.113 \pm 0.013$	79 ± 84	69.9 ± 1.3	94.4 ± 2.7	5.75
31[b]ba	LDN 1689 IRS 5Ba	$\cdots$	16:31:51.929–24:56:17.44	$\cdots$	$\cdots$	<1	<1	<0.06
31[b]bb	LDN 1689 IRS 5Bb	$\cdots$	16:31:51.915–24:56:17.376	$0.129 \pm 0.025 \times 0.047 \pm 0.037$	117 ± 17	4.39 ± 0.16	5.47 ± 0.33	0.34
32	WSB 74	$\cdots$	16:31:54.700–25:03:24.000	$\cdots \times \cdots$	$\cdots$	$\cdots$	<0.71	<0.04
33[a]a	DoAr 51A	$\cdots$	16:32:11.848–24:40:21.90	$\cdots \times \cdots$	$\cdots$	$\cdots$	<0.75	<0.05
33[a]b	DoAr 51B	$\cdots$	16:32:11.904–24:40:21.76	$\cdots \times \cdots$	$\cdots$	$\cdots$	<0.75	<0.05
34[a]a	L1689-IRS 7A	II	16:32:21.047–24:30:36.309	$0.080 \pm 0.012 \times 0.066 \pm 0.021$	144 ± 66	29.17 ± 0.5	33.43 ± 0.96	2.03

Table 4
(Continued)

Index	Object	Class	Derived Position (J2000)	Disk Size (″)	Disk PA (°)	Peak Flux (mJy beam^{-1})	Integrated Flux (mJy)	M_{disk} ($M_{Jupiter}$)
34[a]b	L1689-IRS 7B	II	16:32:20.811–24:30:29.487	0.110 ± 0.015 × 0.066 ± 0.038	156 ± 28	5.16 ± 0.13	6.32 ± 0.25	0.39
35	Haro 1-17	II	16:32:21.928–24:42:15.208	0.135 ± 0.016 × 0.064 ± 0.023	79 ± 12	6.97 ± 0.2	8.87 ± 0.41	0.53
36[a,e]	2MASS J16335560-2442049AB	II	16:33:55.610–24:42:05.370	0.670 ± 0.084 × 0.461 ± 0.059	77 ± 15	24.9 ± 2.7	233 ± 28	14.17
38[c,d]	WSB 82	II	16:39:45.440–24:02:04.250	1.301 ± 0.057 × 0.632 ± 0.028	171.6 ± 2.2	17.44 ± 0.72	437 ± 19	26.52
39	2MASS J16214513-2342316	I	16:21:45.122–23:42:32.182	0.628 ± 0.032 × 0.118 ± 0.014	174.33 ± 0.97	21.73 ± 0.81	94.3 ± 4.3	5.73
40	2MASS J16263682-2415518a	F	16:26:36.827–24:15:52.298	0.390 ± 0.046 × 0.323 ± 0.041	6.1 ± 28.3	10.17 ± 0.83	46.3 ± 4.5	2.82
41	WL6	I	16:27:21.791–24:29:53.826	0.106 ± 0.019 × 0.072 ± 0.027	16 ± 28	15.33 ± 0.37	18.73 ± 0.73	1.14
42	GY 312	I	16:27:38.936–24:40:21.058	0.390 ± 0.009 × 0.121 ± 0.007	168.27 ± 0.94	34.45 ± 0.56	92.9 ± 2	5.66
43	2MASS J16274161-2446447	I	16:27:41.601–24:46:45.082	0.267 ± 0.011 × 0.139 ± 0.009	99.8 ± 3.1	14.75 ± 0.32	31.3 ± 0.95	1.90
44	GY 344	...	16:27:45.800–24:44:54.000	... × ...	...	...	<0.74	<0.04
45[a]a	YLW 52a	F	16:27:51.796–24:31:46.048	0.216 ± 0.043 × 0.106 ± 0.066	129 ± 17	3.13 ± 0.28	5.46 ± 0.72	0.34
45[a]b	YLW 52b	F	16:27:51.479–24:31:40.33		...	<0.7	<0.7	<0.03
46	WSB 60	II	16:28:16.503–24:36:58.463	0.554 ± 0.026 × 0.512 ± 0.025	135 ± 27	26.31 ± 0.98	232.2 ± 9.6	14.17
47	2MASS J16313383-2404466	F	16:31:33.831–24:04:47.036	<0.16 × 0.057	...	4.4 ± 0.24	5.52 ± 0.48	0.34
48	IRS 63	F	16:31:35.659–24:01:29.893	0.521 ± 0.024 × 0.359 ± 0.018	150 ± 5.2	123.5 ± 4.8	776 ± 35	47.19
49	2MASS J16442430-2401250	...	16:44:24.300–24:01:25.000	... × ...	...	...	<0.80	<0.05
50	Haro 1-11	II	16:27:38.325–23:57:32.936	0.151 ± 0.020 × 0.113 ± 0.021	84 ± 30	7.61 ± 0.28	11.21 ± 0.62	0.68

Notes.
[a] Field is a binary source.
[b] Field is a triple source.
[c] Transition disk.
[d] Evidence of gap in the disk.
[e] Circumbinary disk.
[f] Potential circumbinary disk.

Table 5
Statistics of Various Comparisons

Comparison	Flux p-value
Singles	0.00434
Binaries	0.70718
Triples	0.18367
Multiples	0.23964
Class I	0.00122
Class II	0.50860

Taurus Population	Median Flux (mJy)
Singles	57.4
Binaries	10.7
Triples	29.2
Multiples	12.9
Class I Sources	115.8
Class II Sources	21.4

Note. Comparison of the various p-values obtained from each CDF. Note that "multiples" is a combination of both binary and triple systems.

5.2. Disks in Binary Systems and Tidal Truncation

Protoplanetary disks in binary systems are subject to far more interactions than disks in single systems, due to the manner in which disks around stars and stellar companions interact. The disks surrounding these protostars can only grow to a certain radius before that material is stripped away by its companion. This is likely due to the interactions with their companions, yielding a loss of disk material (Jensen et al. 1996; Harris et al. 2012). The lower disk fluxes can be interpreted as being due to lower disk masses. Theory indicates that disk truncation in binaries is particularly sensitive to the binary's semimajor axis a and eccentricity e. Essentially, the closer the periastron distance $d = a(1 - e)$, the more severe the truncation. We use the analytic model described in Pichardo et al. (2005) to estimate the equilibrium truncated radius of our binary sources. This model yields a prediction for a circumstellar disk's truncation radius given its host binary's orbital elements a and e, as well as the mass ratio q, which we assume to be unity (this has little effect, as the truncation radius depends only very weakly on q for reasonable values of q). Because we have no orbital information on our binary systems outside of a projected separation on the sky, we implement a statistical method to estimate the true orbital elements a and e based on the projected separation of the two stars; for details, see Harris et al. (2012). We then convert this to a prediction for the tidal radii. The detailed predictions are somewhat sensitive to the choice of the eccentricity probability density function; we choose a uniform distribution picking e between 0 and 1 for this. As seen in Figure 13, all of our sources, barring the two with upper limit detections, are well below the equilibrium line. This means that for the binary systems we observed in Oph, truncation is not responsible for the disk size observed. This is in contrast to what Harris et al. (2012; see their Figure 11) found for the Taurus binary systems. The Taurus systems have a much more scattered distribution, with points both above and below the equilibrium.

Figure 13 shows that the measured dust disk radius and that predicted from our statistical modeling disagree. However, there are two caveats to this analysis. First, the gas and dust extents are not necessarily the same. Dust-size-dependent

aerodynamic effects such as radial drift can lead to differences in the structure of the gas (which comprises the bulk of the disk mass) and that of the large particles responsible for the millimeter continuum emission (e.g., Weidenschilling 1977; Pérez et al. 2012). Due to these effects, the dust emission extent is expected to be more compact than the gas-line emission, with theoretical estimates of the ratio of 0.88 mm continuum extent to CO emission line extent ranging between 1.5 to about 4 (e.g., Facchini et al. 2017). Observational evidence also suggests this to be the correct range (e.g., Andrews et al. 2012; van der Plas et al. 2017). Accordingly, the measured radii could be corrected by a typical correction factor of ∼2–3 and be brought into good agreement with truncation models. Alternatively, because our predictions for the tidal radii are dependent on the (unknown) eccentricity distribution for pre-main-sequence binaries, it is plausible that an eccentricity distribution weighted more toward moderate to high eccentricity would alleviate the discrepancy we note. For main-sequence stars with periods $P \gtrsim 100$ days, observations are consistent with a uniform distribution between 0 and 1 (Duchêne & Kraus 2013). It is plausible that, in the past, the progenitors of these systems (and the analog of the disk-bearing systems we focus on here) had higher eccentricities that were subsequently damped due to star/disk interaction (e.g., Artymowicz & Lubow 2001), making the higher-eccentricity distribution the more appropriate one to use here.

5.3. Transition and Gapped Disks

An interesting outcome of this ALMA survey is how diverse the YSO population we observed is. As discussed in Section 2, our aim was to probe more evolved protostars, to characterize their disks. Of the 49 stellar systems we observed, 5 include transition disks (see Figure 4). Our ALMA observations were only ∼36 s and provide unprecedented detail in all five of these sources. Three of these are known transition disks that have been heavily observed and studied in both the infrared and the sub-/millimeter regimes (ROph 13, ROph 29, ROph 36). One source, ROph 3, does not have existing sub-/millimeter observations, but was determined to be a transition disk from IR data. Finally, ROph 38 has no existing millimeter data, and, unlike the other transition disks observed in this survey, there is no indication of a central cavity in the broadband *Spitzer* near to mid-infrared photometry taken during the C2D survey (Evans et al. 2003). However, we detect a large millimeter cavity, as well as a gap and a ring-like structure of low-level emission surrounding it. This indicates that, while the central cavity may be devoid of millimeter-sized particles, it is *not* devoid of small particles.

The detection of disks that show evidence for narrow gaps in their emission is a particularly exciting result from our survey. Such gaps in the millimeter emission from the disk have been directly imaged previously in the young Class I/II object HL Tau (ALMA Partnership et al. 2015) and the nearby older Class II TW Hya (Andrews et al. 2016; Nomura et al. 2016), as well as in the higher-mass Herbig Ae stars HD 163296 (Isella et al. 2016) and HD 169142 (Fedele et al. 2017). Modeling of ALMA continuum data at 0.87 and 1.3 mm of the young Class II star AA Tau also suggests multiple gaps in this star's disk (Loomis et al. 2017). The leading candidates for how the gaps open are either that a forming protoplanet/gas-giant core gravitationally torques material around it, effectively repelling
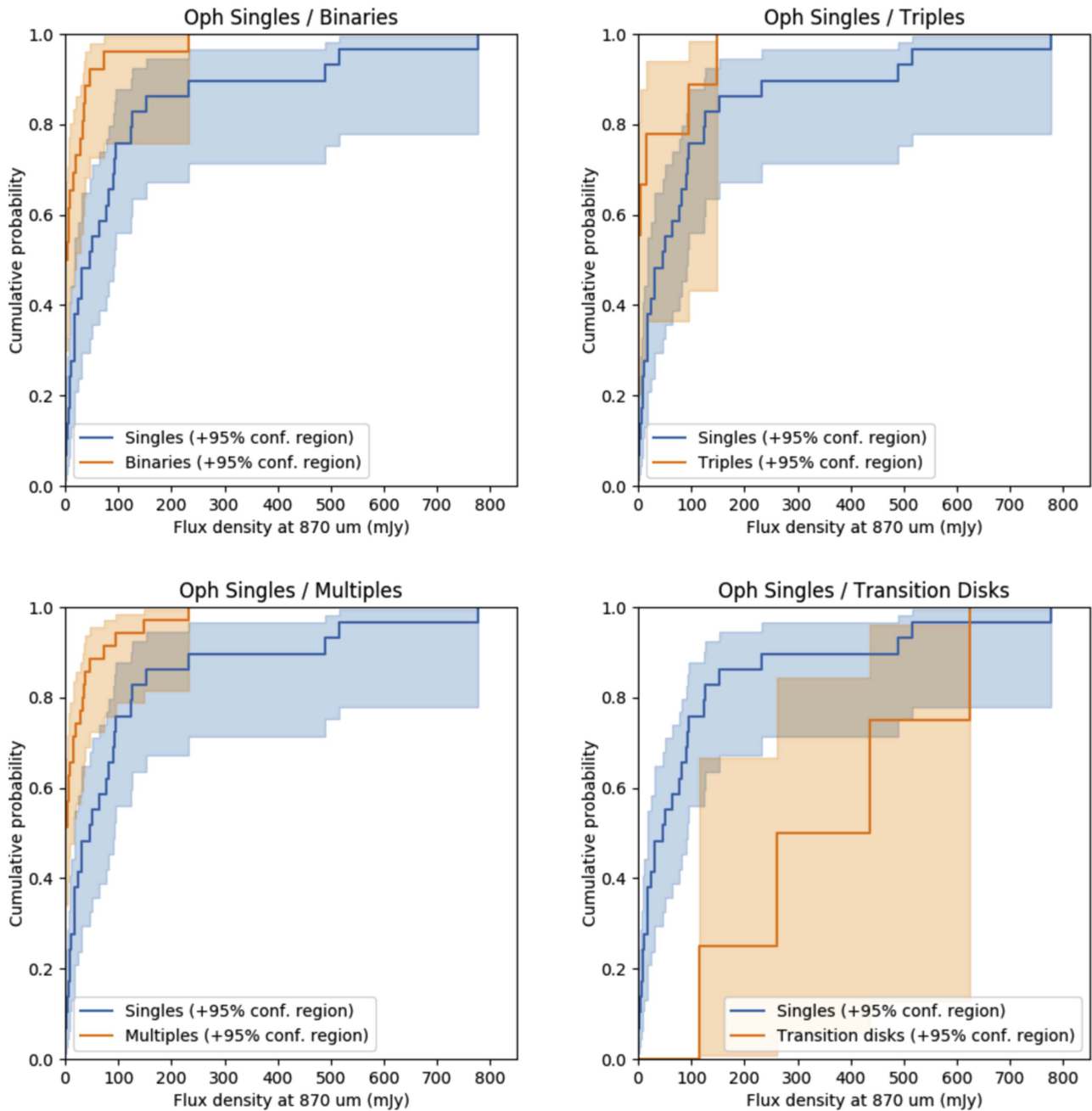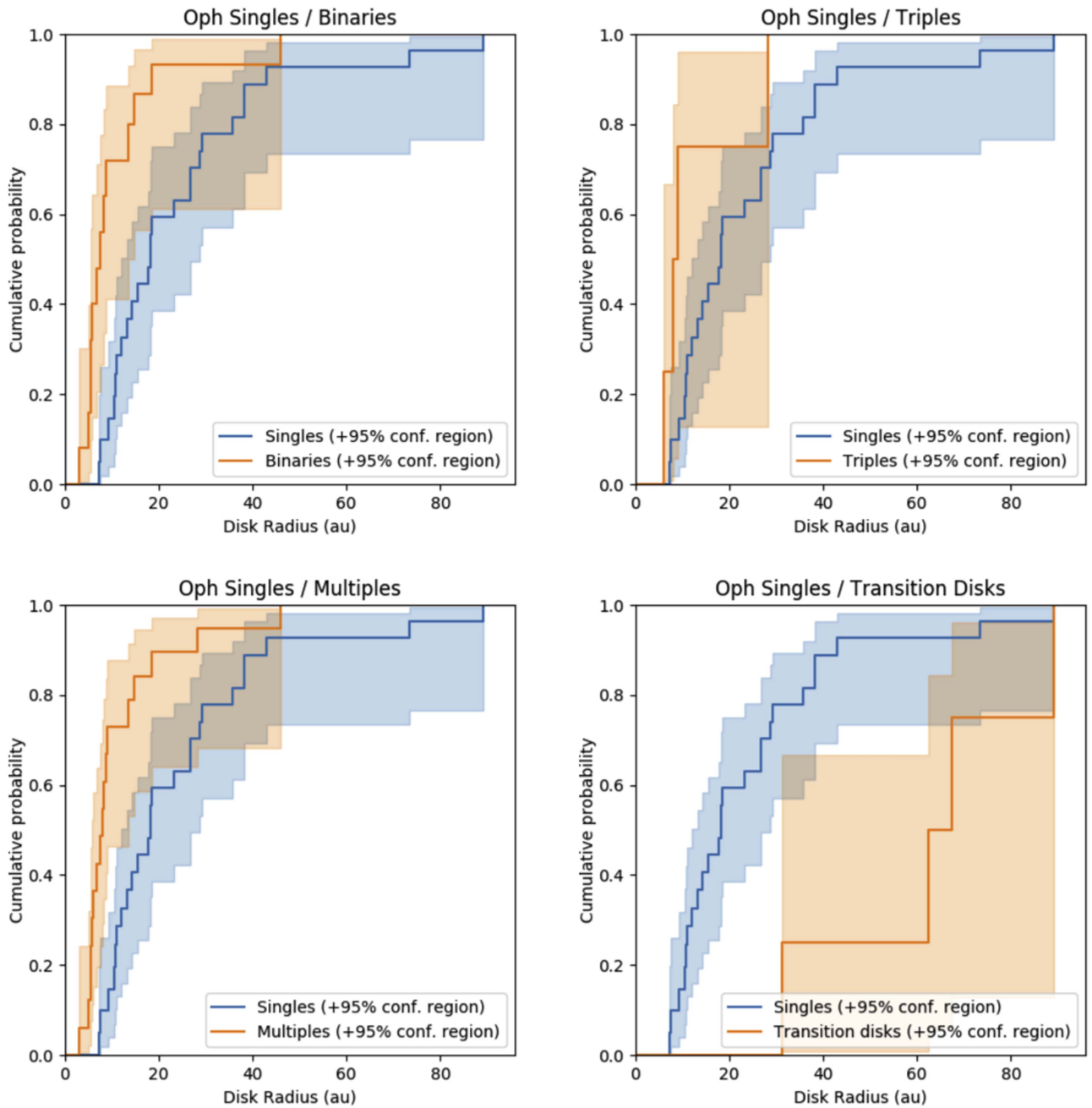
Figure 5. CDF flux comparisons between the single population of protostars in ρ Ophiuchus and the other multiplicities. The shaded area is taking into account the upper limits of the various fluxes. Note that the transition disks are only included in that category and not in the singles or triples.

some disk material away from it (Lin & Papaloizou 1986), or through enhanced grain growth due to pressure bumps caused by planets (Birnstiel et al. 2010). Other suggestions from theorists for forming rings and gaps in the millimeter emission include dust sintering (Okuzumi et al. 2016) and disk-surface density variation driven by inhomogeneous magnetic field distribution (e.g., Flock et al. 2015) or magnetic disk-winds (Suriano et al. 2017). The exact details of the gap-opening, including the gap structure's dependence on planetary embryo mass and surrounding disk structure, have not been fully analytically described (Crida et al. 2006). In fact, it is uncertain

whether a single planet per gap is required for gap formation or if a single planet can carve multiple gaps (Dong et al. 2017). It is, however, generally agreed that higher embryo masses carve more substantial gaps. Numerical calculations indicate that a range of planetary masses $\gtrsim 0.2 M_{\rm Jupiter}$ can carve observable gaps in disks' millimeter emission.

In our sample, we find two sources, ROph 9 (Elias 24) and ROph 38 (WSB 82), that exhibit clear evidence in the images of substantial disk gaps (see Figures 1 and 4), while another source, ROph 8 (DoAr 25; see Figure 1) shows some evidence of a potential gap in the disk in its image. We present these

Figure 6. Radius CDF comparisons between the single population of protostars in ρ Ophiuchus and the other multiplicities. The shaded area is taking into account the upper limits of the radii. Note that the transition disks are only included in that category and not in the singles or triples.

sources again in Figure 14 with an altered color scale to emphasize the gaps and low-lying emission in each disk. To quantify the structure of the gaps, we follow the procedure used by ALMA Partnership et al. (2015) to study the gap structure in the millimeter emission of HL Tau and deprojected each image using the fit disk center, inclination, and position angle, and produce azimuthally averaged surface brightness profiles. These profiles are shown in Figure 15.

In the cases of ROph 9 and 38, there are obvious deficits of emission observed at approximately 65 and 170 au, respectively. These gaps appear to be either unresolved or only marginally resolved by the synthesized beam of the array.

There is a hint of a plateau in the profile for ROph 8, which, when combined with the imaging results, suggest a potential deficit in emission at approximately 95 au. Because the gaps are only marginally resolved, they must be less than about 10 au in annular extent. To ensure that we are not "missing" sources that may have gaps that are not obvious in the images, we constructed these deprojected profiles for each source in our sample. Each source without obvious evidence for a millimeter cavity (see Figure 4) shows a monotonically decreasing flux density with radius until the flux density starts to approach the noise level in the images. We will present a more in depth analysis of both the transitional disks and the gapped disks in a
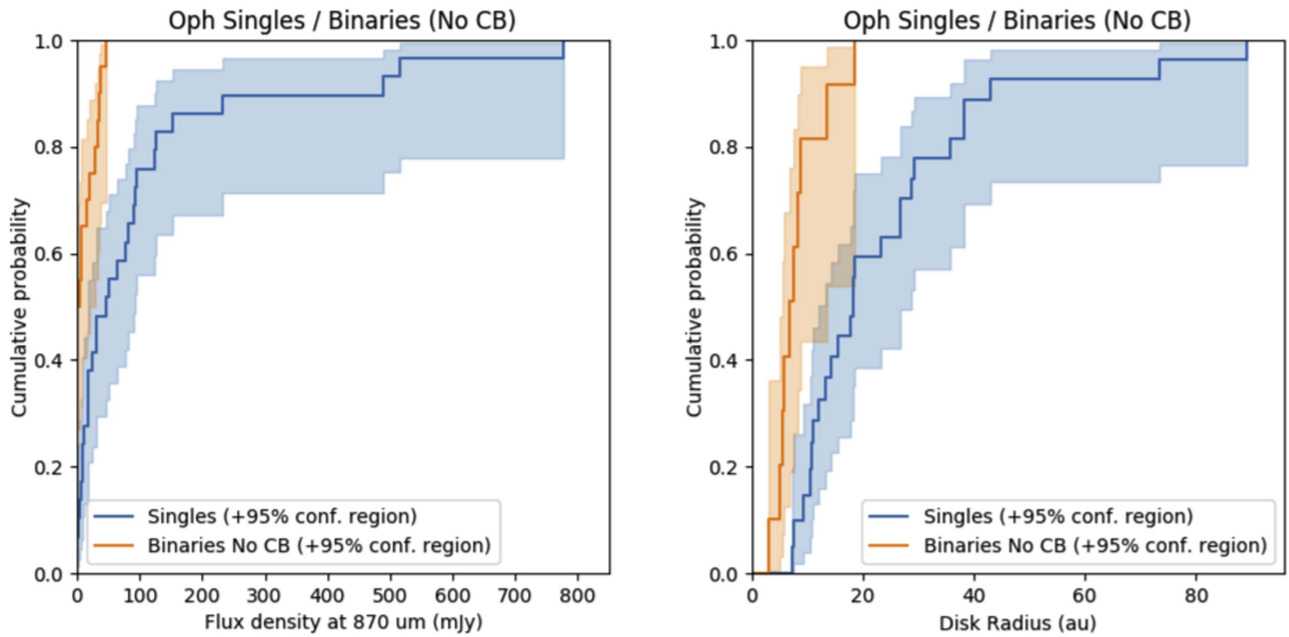
Figure 7. CDF comparing the single and binary population of ρ Ophiuchus, this time with the circumbinary disks taken out of the sample. Note how different the two populations are when the circumbinary disks are taken out of the binary sample.
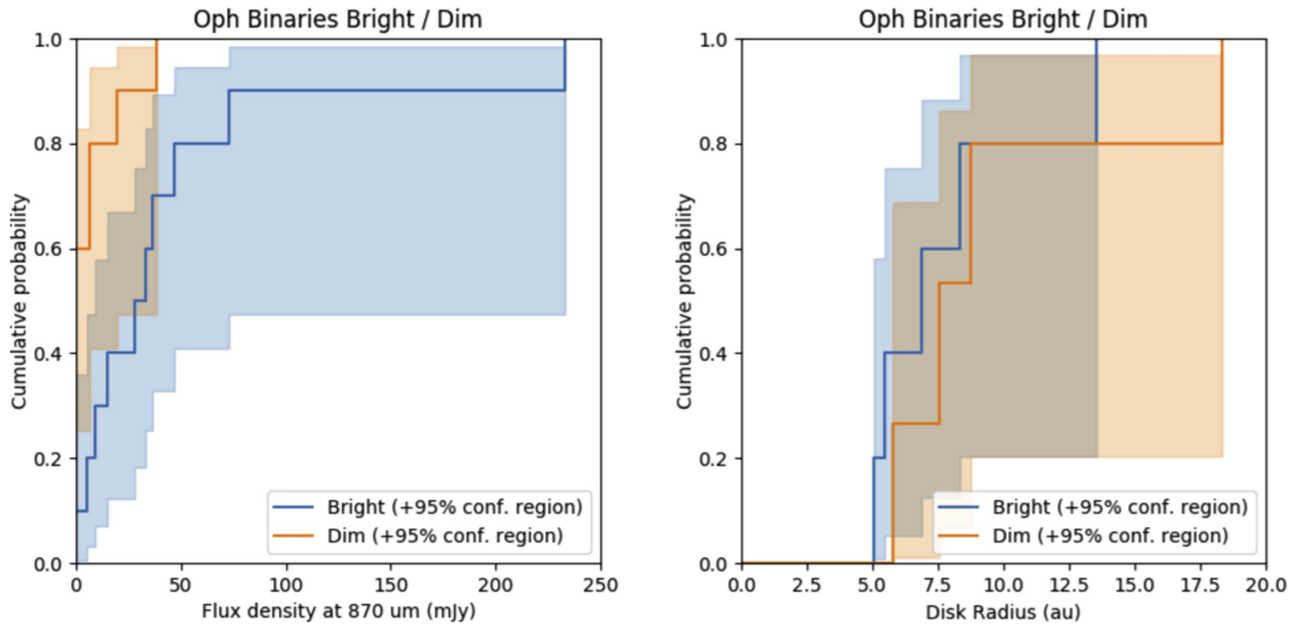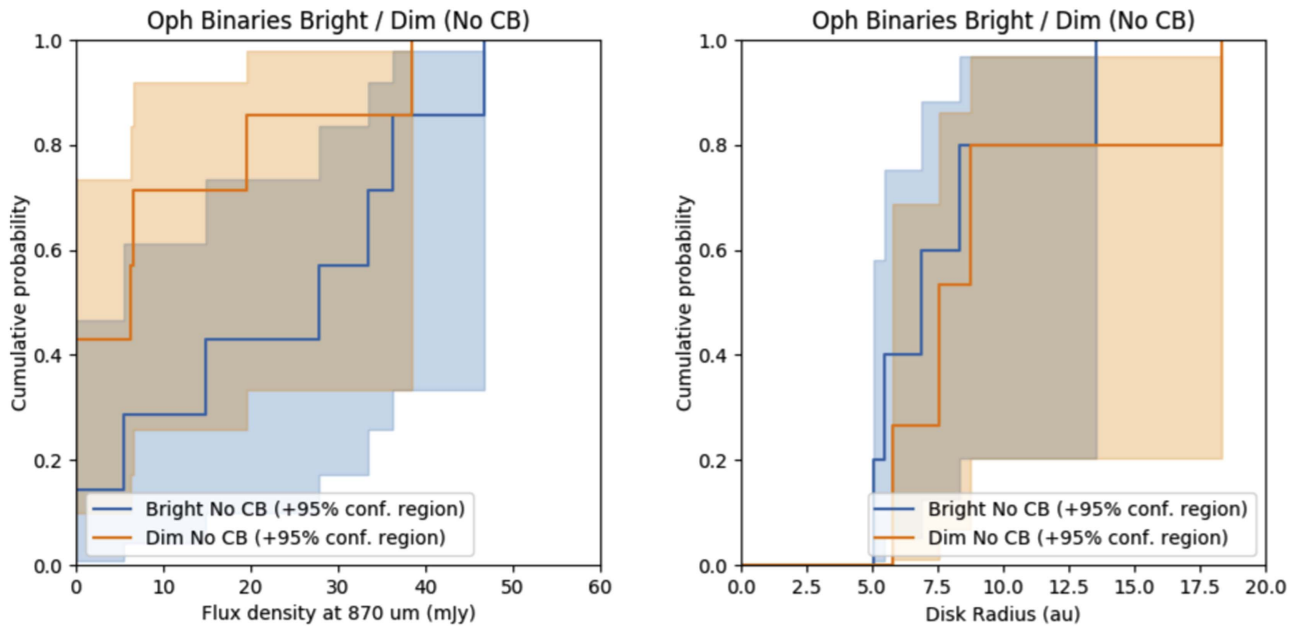

Figure 8. CDF comparisons of both flux and radius for the brighter and dimmer component of the binary protostar population in ρ Ophiuchus.

future work.

One potentially interesting question we can begin to ask is the fraction of disks (f) that show ongoing, present-day evidence for planet formation. If we consider either disk gaps or large millimeter cavities (in the absence of other explanations, such as known binarity) as evidence of ongoing planet formation, we find that 6 out of 49 disks in our sample show evidence of forming planets that are massive enough to open up large gaps or cavities at the current epoch. This yields an estimate of $f = 0.122$, with a 95% confidence interval of $0.031 < f < 0.21$. Note that f represents the fraction of systems that are estimated to have large ($\gtrsim 0.2 M_{\rm Jupiter}$) mass reservoirs that also have signposts of planet formation (i.e., gaps or central cavities).

5.4. Asymmetric Dust Disks

Asymmetries in the millimeter continuum emission from circumstellar disks have recently become of interest due to their likely origin in dust traps that may enable rapid grain growth past the barriers that, e.g., radial drift may impose (Pinilla et al. 2012; Miranda et al. 2017; Ragusa et al. 2017). These asymmetries are sometimes observed in transitional disks as a potential sign of a planet forming an azimuthally asymmetric pressure gradient within the surrounding disk (e.g., IRS 48, van der Marel et al. 2013; SAO 206462 and SR 21, Pérez et al. 2014). In each of our sample of transitional disks, we also observe somewhat substantial asymmetries in the outer disk, with a typical contrast of about 20% from

Figure 9. CDF comparisons of both flux and radius for the brighter and dimmer component of the binary protostar population in ρ Ophiuchus, without circumbinary disks.
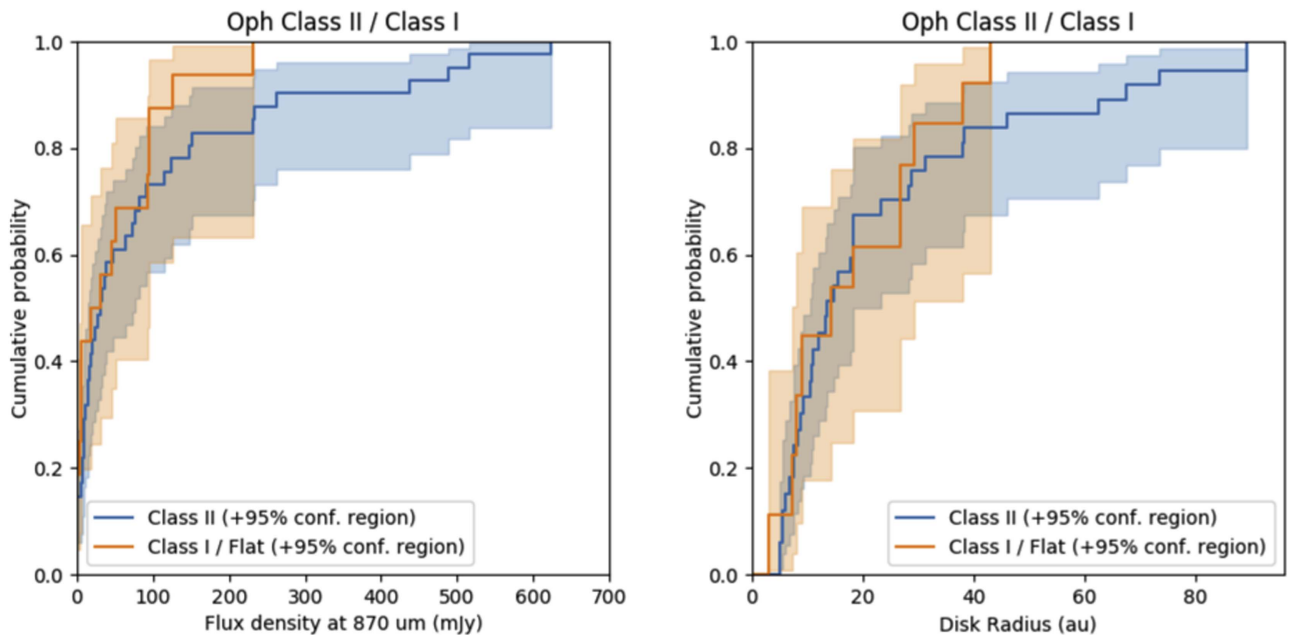
Figure 10. CDF comparisons of both flux and radius for Class II sources and Class I/Flat sources in ρ Ophiuchus.

maximum to minimum in the profile of brightness versus azimuth as a given disk radius. In addition to the transitional disks we identify on the basis of a substantial millimeter cavity in Figure 4, we also identify the primary disk in one of our binaries, ROph 40, as having a large asymmetry in its continuum emission. It is shown in Figure 16. This source shows no infrared signature of being a transitional disk in either *Spitzer* or *Herschel* data. Furthermore, any cavity in the millimeter emission is not obvious, unlike in the analogous case of ROph 38. However, the asymmetry in the dust emission is reminiscent of what is observed in the transitional disks both we and others have mapped in the millimeter. Unfortunately, we do not have coverage of the requisite gas-line emission to be able to tell whether this is a true dust trap

or a mere asymmetry in the overall mass distribution of the source.

6. Summary

We have presented an ALMA imaging survey of the 870 μm dust continuum emission from the circumstellar material of 49 systems in the ρ Ophiuchus molecular cloud complex. These systems, having been selected on the basis of excess in each of the *Spitzer* IRAC and MIPS bands, represent the stellar systems most likely to have sufficient circumstellar material to enable planet formation over the next few Myr. This survey, observing each source only for 36 s per source, shows the versatility and promise of the ALMA instrument for studies in star and planet
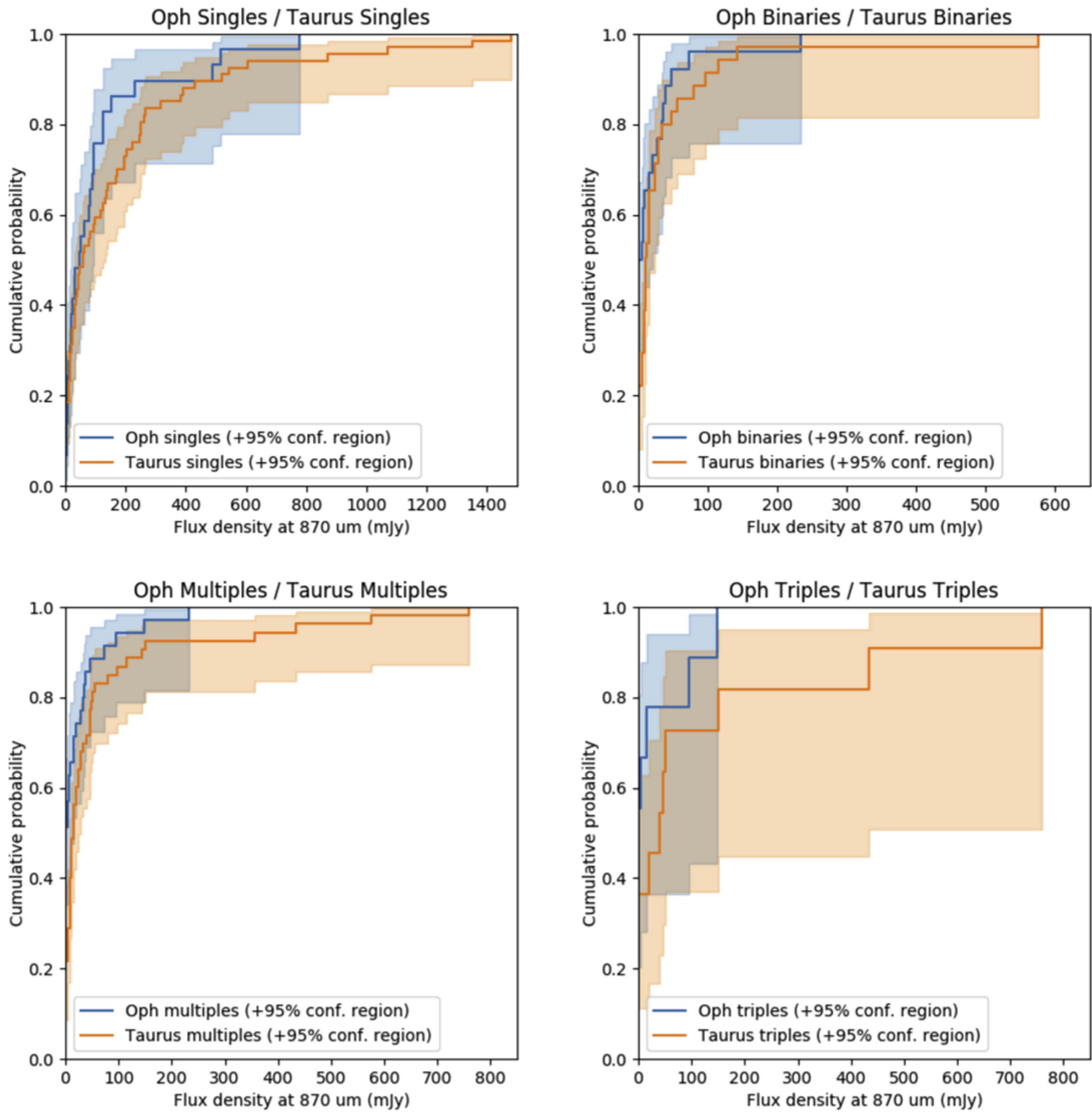
Figure 11. CDF comparisons of flux in ρ Ophiuchus and Taurus for isolated protostars, binaries, triples, and multiples (binaries plus triples).

formation. Many of these sources represent low-mass targets that have not been observed at millimeter wavelengths before. We summarize our results and analysis below.

1. We divided the sources into several different populations (i.e., single stars, binaries, triple systems, and transition disks) and computed Kaplan–Meier product limit estimators to estimate the cumulative probability distribution for both disk flux and disk radius for each population. We find significant differences in both flux and radius among the singles and binaries in Oph: disk fluxes and radii in binaries are significantly smaller than in single stars. Similar results about the fluxes have been noted previously (e.g., Jensen et al. 1994, 1996; Harris et al. 2012), but disk radii at millimeter wavelengths have

never explicitly been found to be smaller in disks in binaries compared to disks around isolated stars. Large differences in circumstellar mass (for which, assuming a single temperature and κ, flux can be a proxy for) and radius over a small range of ages illustrate the diversity of conditions in the disk, wherein planets are forming.

2. The lack of flux in the binary population is typically considered to be due to either disk truncation after formation, or caused by something that sets the disk radii during formation. Using a statistical model to convert from projected separation to semimajor axis and eccentricity, we computed the distribution of expected truncation radii using the analytic prescription of Pichardo et al. (2005) for each disk. We found that the (dust) disks in our sample are much too small to have
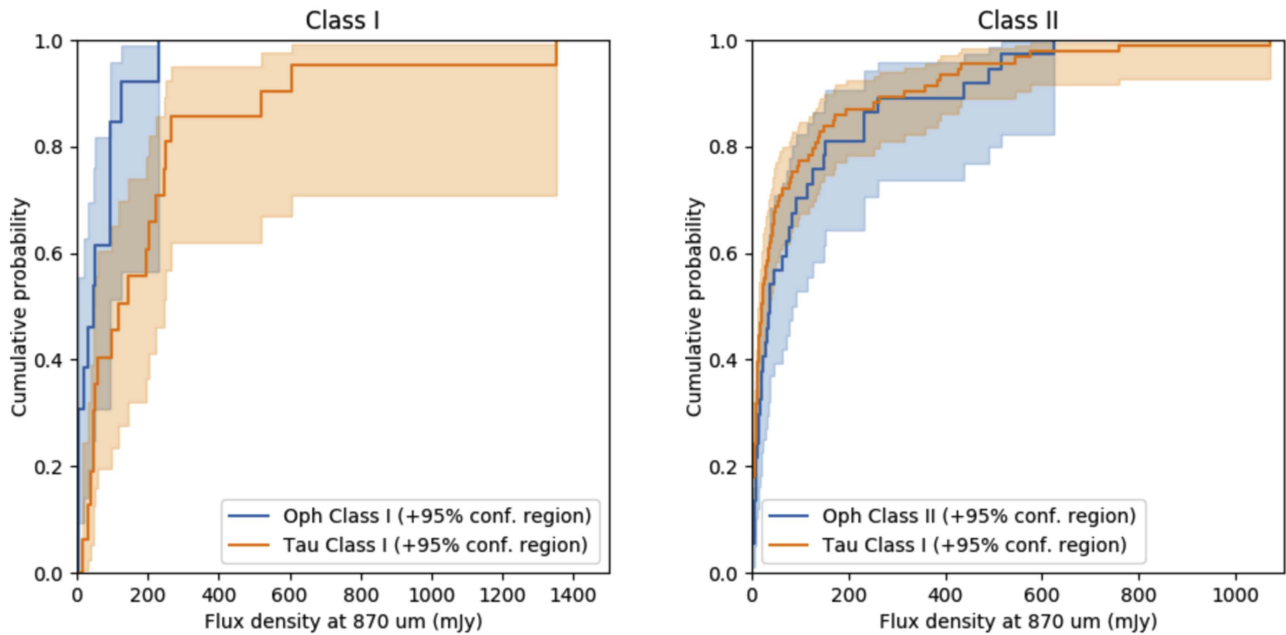
Figure 12. CDF comparisons of flux in ρ Ophiuchus and Taurus for Class I and Class II protostars.
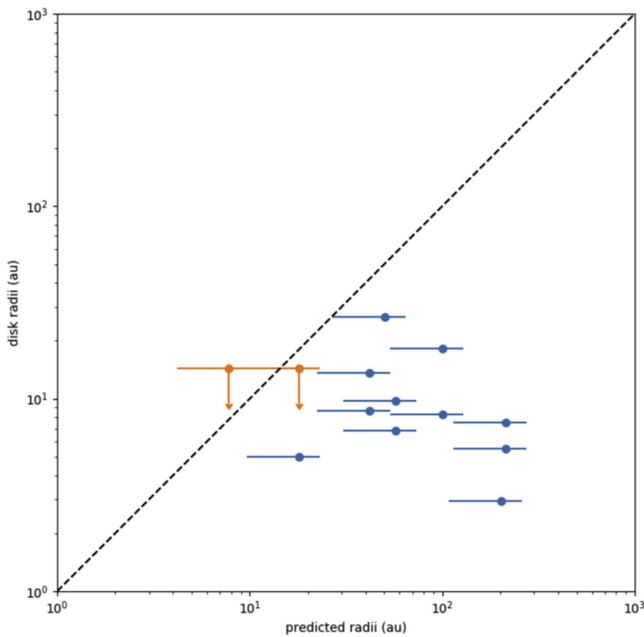
Figure 13. Measured disk radii in the binary systems observed (see Table 4) compared with the expected disk radii based on tidal interaction models from Pichardo et al. (2005). Note that the expected disk radii are lower than the equality line, meaning that disk truncation is not setting the disk radii in ρ Ophiuchus. The orange arrows represent the two sources for which we have upper limits on the radius. The error bars on the points represent the 68% confidence region.

been significantly affected by tidal truncation. This could have a natural explanation, as the gas disk extent is expected to a $\sim$ a few times larger than the dust disk extent. On the other hand, if this is not the case, it could suggest that the smaller disk radii in the binary systems are primordial, rather than a product of binary interaction after disk formation. This may be counterintuitive, because binary systems tend to have larger angular momenta than single systems. One possibility is that most

of the angular momentum of a binary system is stored in the binary orbit, leaving less for the circumstellar disks. In any case, this is an intriguing result that disk and binary formation theories should seek to address.

3. We detected several transition disks, two of which are the first ever millimeter observations (ROph3 = 2MASS J16230923-2417047; ROph 38 = WSB 82), whereas one (ROph38 = WSB 82) is being classified as a transition disk for the first time based solely on the presence of a millimeter cavity unexpected from the available infrared data. In particular, WSB 82 is a transition disk with a noticeable gap in the low surface brightness outer disk that resembles the gaps seen in ALMA images of other Class II disks so far (e.g., HL Tau, ALMA Partnership et al. 2015, HD 163296, Isella et al. 2016, and TW Hya, Andrews et al. 2016). Interestingly, we find an intriguing trend that the transition disks are on average much brighter and larger than both Class I and Class II disks. Theoretical studies of disk evolution need to account for this trend.

4. We have discovered an unexpected millimeter companion to the Class II source WLY 2-69 at $7''56$ ($\sim$1000 au); given the density of millimeter-wave background sources, it is most likely physically associated with the source. A search of the literature on multiplicity in Oph yielded no reports of an optical or infrared companion. An examination of archival images from *Spitzer*, however, shows this companion source in the infrared.

Due to the sheer number of baselines available, as well as the very sensitive receivers on the antennas, ALMA is producing exciting results almost daily, particularly in the study of protoplanetary disks. Surveys such as this one of 49 targets in ρ Ophiuchi, as well as that of a set of 92 sources in the σ Ori cluster (Ansdell et al. 2017), demonstrate conclusively that ALMA as a rapid survey instrument is coming into its own.
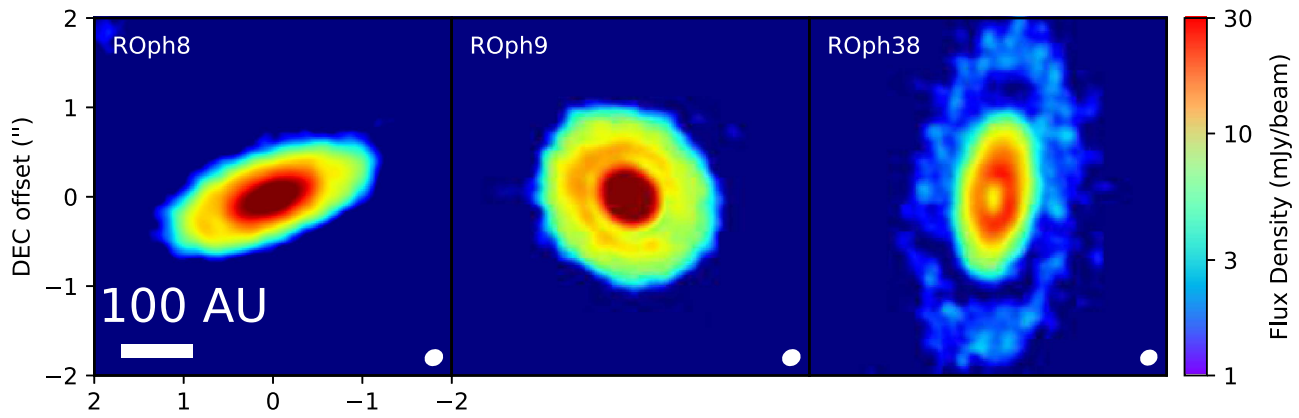
Figure 14. ROph 8, ROph 9, and ROph 38, the candidate gapped disks imaged in our survey. Note that the color scale is saturated to more clearly show the gaps.
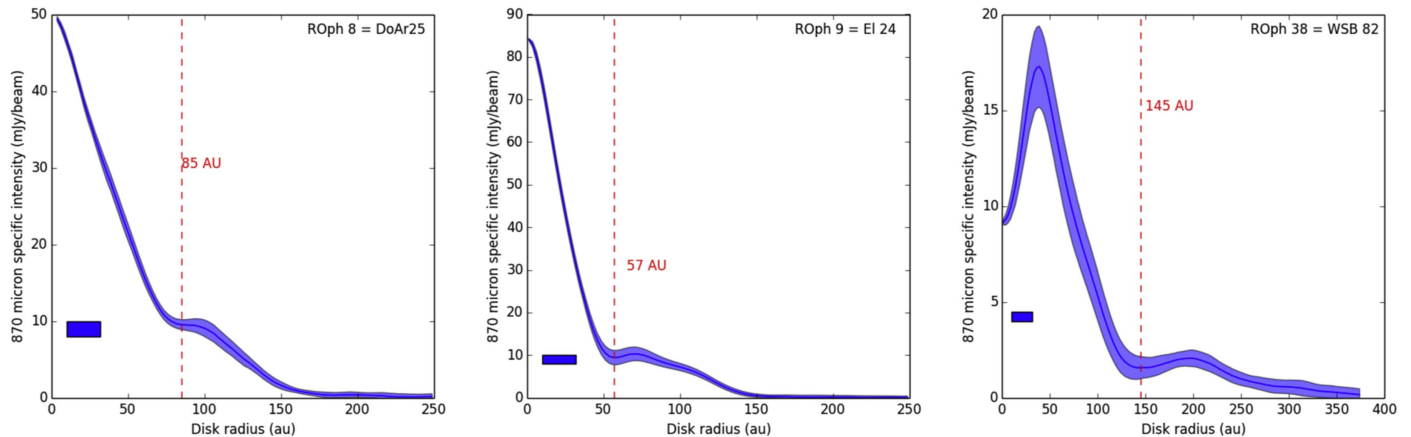

Figure 15. Deprojected, azimuthally averaged surface brightness profiles for three sources in our survey with evidence for gaps. For ROph 9 and 38, the entire 2π in azimuth is averaged, whereas for ROph 8, only the region within $20°$ of the disk major axis is averaged (due to the high disk inclination, the deficit in emission is seen only along the major axis). The resolution is shown as a thick horizontal bar. The estimated locations of the gaps are shown by red dashed vertical lines.
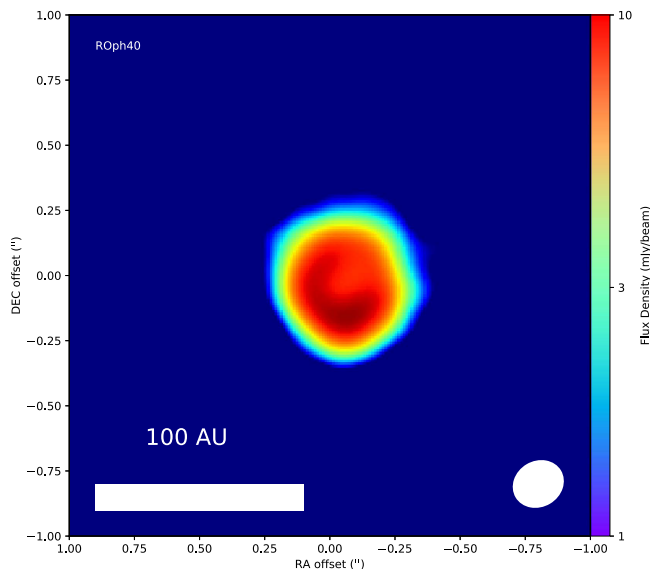
Figure 16. Map of the 870 μm continuum emission from the disk in the ROph 40 (ISO-Oph 51) binary system. The color scale has been altered to emphasize the asymmetric dust emission and "horseshoe" shape in the emission.

ORCID iDs

Erin G. Cox ⓘ https://orcid.org/0000-0002-5216-8062
Leslie W. Looney ⓘ https://orcid.org/0000-0002-4540-6587
Hsin-Fang Chiang ⓘ https://orcid.org/0000-0002-1181-1621
Claire Chandler ⓘ https://orcid.org/0000-0002-7570-5596
Kaitlin Kratter ⓘ https://orcid.org/0000-0001-5253-1338
Laura Perez ⓘ https://orcid.org/0000-0002-1199-9564
John J. Tobin ⓘ https://orcid.org/0000-0002-6195-0152

References

ALMA Partnership, Brogan, C. L., Pérez, L. M., et al. 2015, ApJL, 808, L3
Andre, P., & Montmerle, T. 1994, ApJ, 420, 837
Andre, P., Montmerle, T., Feigelson, E. D., & Steppe, H. 1990, A&A, 240, 321
Andre, P., Ward-Thompson, D., & Barsony, M. 1993, ApJ, 406, 122
Andrews, S. M., & Williams, J. P. 2005a, ApJ, 631, 1134
Andrews, S. M., & Williams, J. P. 2005b, ApJL, 619, L175

Cox et al.

Andrews, S. M., & Williams, J. P. 2007, ApJ, 671, 1800
Andrews, S. M., Wilner, D. J., Hughes, A. M., et al. 2012, ApJ, 744, 162
Andrews, S. M., Wilner, D. J., Hughes, A. M., Qi, C., & Dullemond, C. P. 2009, ApJ, 700, 1502
Andrews, S. M., Wilner, D. J., Hughes, A. M., Qi, C., & Dullemond, C. P. 2010, ApJ, 723, 1241
Andrews, S. M., Wilner, D. J., Zhu, Z., et al. 2016, ApJL, 820, L40
Ansdell, M., Williams, J. P., Manara, C. F., et al. 2017, AJ, 153, 240
Artymowicz, P., & Lubow, S. H. 1994, ApJ, 421, 651
Artymowicz, P., & Lubow, S. H. 2001, in IAU Symp. 200, The Formation of Binary Stars, ed. H. Zinnecker & R. D. Mathieu (Cambridge: Cambridge Univ. Press), 439
Barsony, M., Koresko, C., & Matthews, K. 2003, ApJ, 591, 1064
Barsony, M., Ressler, M. E., & Marsh, K. A. 2004, AAS Meeting, 36, 156.01
Birnstiel, T., Dullemond, C. P., & Brauer, F. 2010, A&A, 513, A79
Bitsch, B., & Kley, W. 2011, A&A, 536, A77
Bitsch, B., Lambrechts, M., & Johansen, A. 2015, A&A, 582, A112
Bohlin, R. C., Savage, B. D., & Drake, J. F. 1978, ApJ, 224, 132
Cheetham, A. C., Kraus, A. L., Ireland, M. J., et al. 2015, ApJ, 813, 83
Chiang, E., & Laughlin, G. 2013, MNRAS, 431, 3444
Cieza, L. A., Padgett, D. L., Allen, L. E., et al. 2009, ApJL, 696, L84
Cieza, L. A., Schreiber, M. R., Romero, G. A., et al. 2010, ApJ, 712, 925
Crida, A., Morbidelli, A., & Masset, F. 2006, Icar, 181, 587
Davidson-Pilon, C., Kalderstam, J., Kuhn, B., et al. 2017, lifelines.py, v0.11.1, Zenodo, doi:10.5281/zenodo.815943
Dong, R., Li, S., Chiang, E., & Li, H. 2017, ApJ, 843, 127
Duchêne, G., Bontemps, S., Bouvier, J., et al. 2007, A&A, 476, 229
Duchêne, G., Bouvier, J., Bontemps, S., André, P., & Motte, F. 2004, A&A, 427, 651
Duchêne, G., & Kraus, A. 2013, ARA&A, 51, 269
Dunham, M. M., Stutz, A. M., Allen, L. E., et al. 2014, in Protostars and Planets VI, ed. H. Beuther et al. (Tucson, AZ: Univ. Arizona Press), 195
Espaillat, C., D'Alessio, P., Hernández, J., et al. 2010, ApJ, 717, 441
Evans, N. J., II, Allen, L. E., Blake, G. A., et al. 2003, PASP, 115, 965
Facchini, S., Birnstiel, T., Bruderer, S., & van Dishoeck, E. F. 2017, A&A, 605, A16
Fedele, D., Carney, M., Hogerheijde, M. R., et al. 2017, A&A, 600, A72
Flock, M., Ruge, J. P., Dzyurkevich, N., et al. 2015, A&A, 574, A68
Furlan, E., Watson, D. M., McClure, M. K., et al. 2009, ApJ, 703, 1964
Ghez, A. M., Neugebauer, G., & Matthews, K. 1993, AJ, 106, 2005
Greenwood, M., Jr. 1926, The Natural Duration of Cancer. Reports of Public Health and Related Subjects, Vol. 33 (London: HMSO)
Haisch, K. E., Jr., Barsony, M., Ressler, M. E., & Greene, T. P. 2006, AJ, 132, 2675
Haisch, K. E., Jr., Greene, T. P., Barsony, M., & Stahler, S. W. 2004, AJ, 127, 1747
Harris, R. J., Andrews, S. M., Wilner, D. J., & Kraus, A. L. 2012, ApJ, 751, 115
Hartmann, L., Calvet, N., Gullbring, E., & D'Alessio, P. 1998, ApJ, 495, 385
Hildebrand, R. H. 1983, QJRAS, 24, 267
Hughes, A. M., Wilner, D. J., Qi, C., & Hogerheijde, M. R. 2008, ApJ, 678, 1119
Isella, A., Guidi, G., Testi, L., et al. 2016, PhRvL, 117, 251101
Jensen, E. L. N., Mathieu, R. D., & Fuller, G. A. 1994, ApJL, 429, L29
Jensen, E. L. N., Mathieu, R. D., & Fuller, G. A. 1996, ApJ, 458, 312
Kalbfleisch, J. D., & Ross, L. P. 2002, The Statistical Analysis of Failure Time Data (2nd ed.; Hoboken, NJ: Wiley)

Kohn, S. A., Shkolnik, E. L., Weinberger, A. J., Carlberg, J. K., & Llama, J. 2016, ApJ, 820, 2
Kraus, A. L., & Ireland, M. J. 2012, ApJ, 745, 5
Kraus, A. L., Ireland, M. J., Cieza, L. A., et al. 2014, ApJ, 781, 20
Kraus, A. L., Ireland, M. J., Martinache, F., & Hillenbrand, L. A. 2011, ApJ, 731, 8
Lada, C. J. 1987, in IAU Symp. 115, In Star-forming Regions, ed. M. Peimbert & J. Jugaku (Cambridge: Cambridge Univ. Press), 1
Leous, J. A., Feigelson, E. D., Andre, P., & Montmerle, T. 1991, ApJ, 379, 683
Lin, D. N. C., & Papaloizou, J. 1986, ApJ, 307, 395
Loinard, L., Torres, R. M., Mioduszewski, A. J., et al. 2007, ApJ, 671, 546
Loinard, L., Torres, R. M., Mioduszewski, A. J., & Rodríguez, L. F. 2008, ApJL, 675, L29
Lombardi, M., Lada, C. J., & Alves, J. 2010, A&A, 512, A67
Loomis, R. A., Öberg, K. I., Andrews, S. M., & MacGregor, M. A. 2017, ApJ, 840, 23
Luhman, K. L., Allen, P. R., Espaillat, C., Hartmann, L., & Calvet, N. 2010, ApJS, 186, 111
Lynden-Bell, D., & Pringle, J. E. 1974, MNRAS, 168, 603
Mann, R. K., Di Francesco, J., Johnstone, D., et al. 2014, ApJ, 784, 82
McMullin, J. P., Waters, B., Schiebel, D., Young, W., & Golap, K. 2007, in ASP Conf. Ser. 376, Astronomical Data Analysis Software and Systems XVI, ed. R. A. Shaw, F. Hill, & D. J. Bell (San Fransisco, CA: ASP), 127
Miranda, R., Li, H., Li, S., & Jin, S. 2017, ApJ, 835, 118
Nomura, H., Tsukagoshi, T., Kawabe, R., et al. 2016, ApJL, 819, L7
Okuzumi, S., Momose, M., Sirono, S.-i., Kobayashi, H., & Tanaka, H. 2016, ApJ, 821, 82
Ortiz-León, G. N., Loinard, L., Kounkel, M. A., et al. 2017, ApJ, 834, 141
Pérez, L. M., Carpenter, J. M., Chandler, C. J., et al. 2012, ApJL, 760, L17
Pérez, L. M., Isella, A., Carpenter, J. M., & Chandler, C. J. 2014, ApJL, 783, L13
Pichardo, B., Sparke, L. S., & Aguilar, L. A. 2005, MNRAS, 359, 521
Pichardo, B., Sparke, L. S., & Aguilar, L. A. 2008, MNRAS, 391, 815
Pinilla, P., Birnstiel, T., Ricci, L., et al. 2012, A&A, 538, A114
Ragusa, E., Dipierro, G., Lodato, G., Laibe, G., & Price, D. J. 2017, MNRAS, 464, 1449
Ratzka, T., Köhler, R., & Leinert, C. 2005, A&A, 437, 611
Rebollido, I., Merín, B., Ribas, Á, et al. 2015, A&A, 581, A30
Rebull, L. M., Padgett, D. L., McCabe, C.-E., et al. 2010, ApJS, 186, 259
Ricci, L., Testi, L., Natta, A., et al. 2010, A&A, 512, A15
Ruíz-Rodríguez, D., Ireland, M., Cieza, L., & Kraus, A. 2016, MNRAS, 463, 3829
Salyk, C., Pontoppidan, K., Corder, S., et al. 2014, ApJ, 792, 68
Suriano, S. S., Li, Z.-Y., Krasnopolsky, R., & Shang, H. 2017, MNRAS, 468, 3850
Torres, R. M., Loinard, L., Mioduszewski, A. J., & Rodríguez, L. F. 2007, ApJ, 671, 1813
Torres, R. M., Loinard, L., Mioduszewski, A. J., & Rodríguez, L. F. 2009, ApJ, 698, 242
van der Marel, N., van Dishoeck, E. F., Bruderer, S., et al. 2013, Sci, 340, 1199
van der Plas, G., Menard, F., Canovas, H., et al. 2017, A&A, 607, A55
Weidenschilling, S. J. 1977, MNRAS, 180, 57
Wilking, B. A., Gagné, M., & Allen, L. E. 2008, in Handbook of Star Forming Regions, ed. B. Reipurth (Tucson, AZ: Univ. Arizona Press), 351
Williams, J. P., & Best, W. M. J. 2014, ApJ, 788, 59
Willson, M., Kraus, S., Kluska, J., et al. 2016, A&A, 595, A9
Young, K. E., Enoch, M. L., Evans, N. J., II, et al. 2006, ApJ, 644, 326